Front. Mech. Eng. 2018, 13(3): 329–353
https://doi.org/10.1007/s11465-018-0466-1

REVIEW ARTICLE

Le YANG, Shuo WANG, Jianghua FENG

Electromagnetic interference modeling and suppression techniques in variable-frequency drive systems

Abstract Electromagnetic interference (EMI) causes electromechanical damage to the motors and degrades the reliability of variable-frequency drive (VFD) systems. Unlike fundamental frequency components in motor drive systems, high-frequency EMI noise, coupled with the parasitic parameters of the trough system, are difficult to analyze and reduce. In this article, EMI modeling techniques for different function units in a VFD system, including induction motors, motor bearings, and rectifier-inverters, are reviewed and evaluated in terms of applied frequency range, model parameterization, and model accuracy. The EMI models for the motors are categorized based on modeling techniques and model topologies. Motor bearing and shaft models are also reviewed, and techniques that are used to eliminate bearing current are evaluated. Modeling techniques for conventional rectifier-inverter systems are also summarized. EMI noise suppression techniques, including passive filter, Wheatstone bridge balance, active filter, and optimized modulation, are reviewed and compared based on the VFD system models.

Keywords variable-frequency drive (VFD), electromagnetic interference (EMI), motor drive modeling, EMI noise suppression

1 Introduction

The rail vehicle traction system has recently experienced rapid development, as demonstrated by the introduction of various converter topologies and control techniques to power traction areas, all of which aim to achieve an efficient and reliable railway transportation system. Figure 1 shows the block diagram of a conventional alternating current (AC) electric locomotive system. As can be seen, the pantograph delivers power from overhead supply lines to the traction system. The main transformer reduces the AC voltage level and provides galvanic isolation for the traction system. The rectifier then converts AC power to direct current (DC) and feeds it to a DC bus. Finally, the DC power is converted into AC power with the inverters to drive the motor system for traction. In this system, electromagnetic interference (EMI) emissions include conducted EMI and radiated EMI. Radiated EMI emitted by undesired antennas, such as magnetic components and long cables, propagates through space and contaminates other electronic loads. Conducted EMI is mainly caused by a fast changing of voltage over time (dv/dt) and the fast switching of the converters or inverters. As shown in Fig. 1, conducted EMI propagates along the conductors in the circuits throughout the rest of the system. The mechanisms of these EMIs are complicated. Moreover, EMI noise in railway systems reduces the reliability of the system, damages equipment, and endangers lives. In this article, existing EMI studies are surveyed, with a focus on conducted EMI noise.

Recently, power electronic systems have been developed for rail vehicles, and various topologies have been proposed for traction systems [1]. However, in actual applications, the propagation of conducted EMI is made more difficult by the complicated structures of traction systems. Figure 2 shows a two-cell H-bridge boost rectifier-inverter traction system. For safety reasons, the heatsinks of the converters, motor frame, and transformer frame are commonly grounded. Active converters, which generate fast changings of voltage and current over time are considered noise sources. Parasitic capacitance among the bus bar, switches, frames, and the ground provide coupling paths for common-mode (CM) noise. The CM current circulating in the system may induce high-

Received December 11, 2016; accepted May 8, 2017

Le YANG, Shuo WANG (✉)
Electrical and Computer Engineering Department, University of Florida, Gainesville, FL 32611, USA
E-mail: shuowang@ieee.org

Jianghua FENG
CRRC Zhuzhou Institute Co., Ltd., Zhuzhou 412001, China

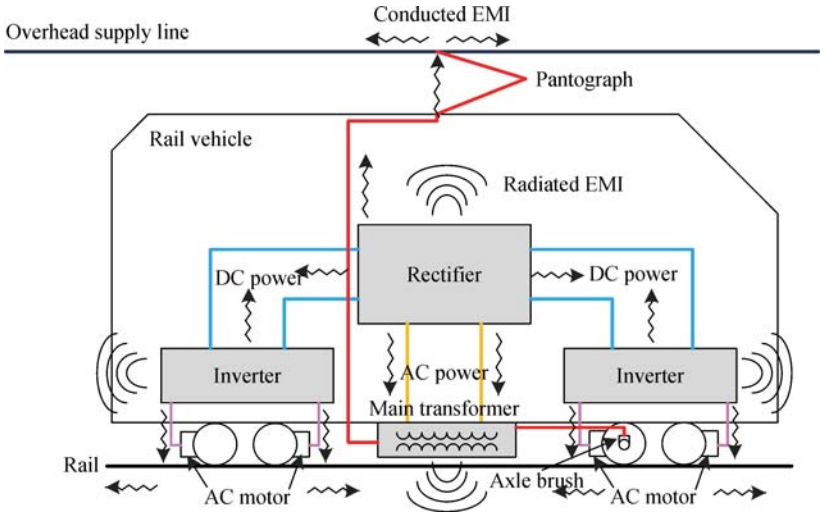

Fig. 1 Block diagram of a rail vehicular system

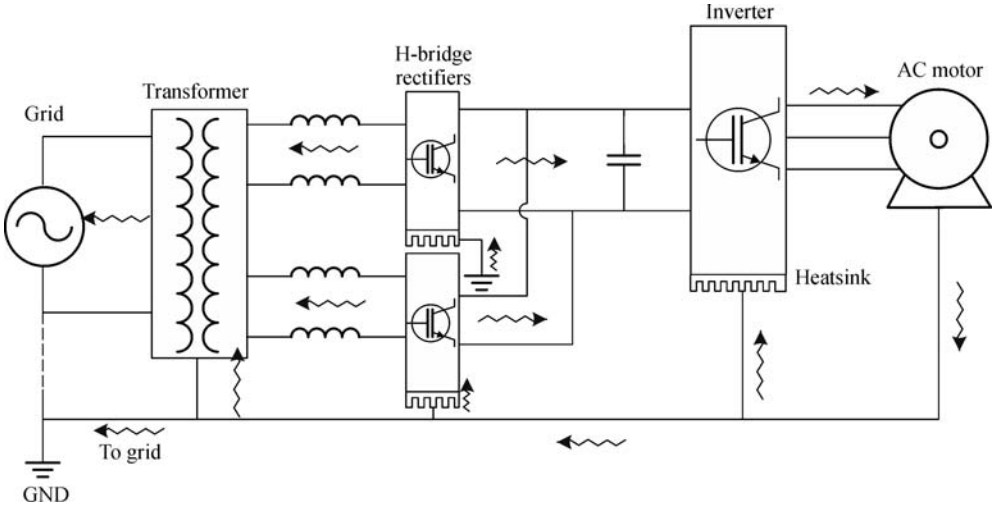

Fig. 2 A motor drive system with a two-cell H-bridge boost rectifier-inverter

frequency resonances and reduce the reliability of the system. Furthermore, the CM current flowing into the grid affects other equipment in the same electrical network.

Figure 3 shows the most commonly used traction system in rail vehicles, which helps us understand EMI issues in power traction systems. This simplified topology includes all the essential equipment and components in a rail vehicle traction system. The three- or single-phase grid provides AC power to the system. A main transformer transforms the high grid voltage into acceptable AC voltages for the traction system. The rectifier, which is either an uncontrollable diode bridge or a controllable active rectifier, then converts AC power into DC power. DC power is fed to the inverter, which provides three-phase power to the AC motor. Conducted EMI noise is studied at frequencies ranging from 9 kHz to 30 MHz. Therefore, EMI researchers aim to develop high-frequency EMI models for converters, inverters, and AC motors. The EMI noise propagation path is determined based on the high-frequency EMI models. Thus, EMI reduction techniques can then be proposed based on such high-frequency EMI models.

The variable-frequency drive (VFD) system and pulse-width modulation (PWM) converters are widely used in rail vehicle applications because of their flexible control and excellent electromechanical performance. However, due to the high dv/dt generated by the high-speed active switches in rectifier-inverters, EMI issues significantly affect motor drive performance and cause potential safety issues. Overvoltage (or overshoot) in motor terminals is one of the problems caused by the mismatch between the cable and the motor impedance under high dv/dt excitations. This transient overvoltage has been observed in the PWM motor drive systems in past studies [2,3]. The amplitude of overvoltage mainly depends on cable length, the PWM voltage rising time, and impedance mismatch

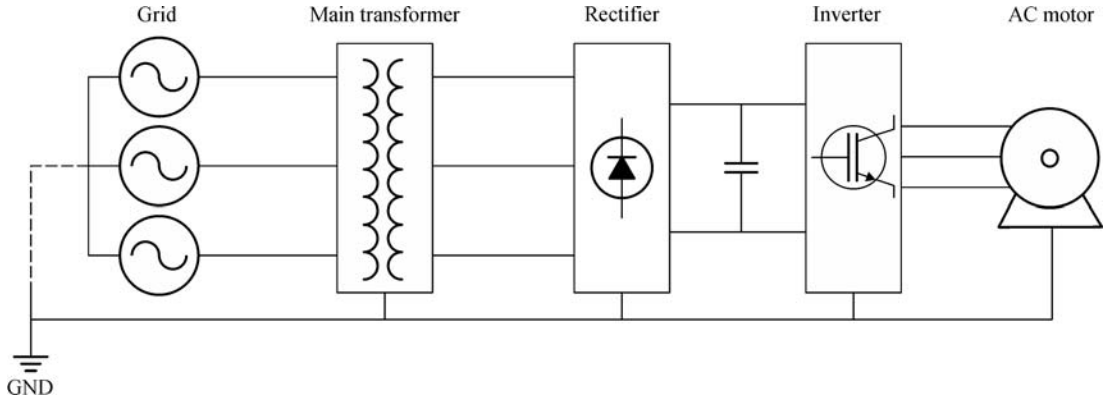

Fig. 3 A commonly used rectifier-inverter system for EMI analysis

between the cable and the motor [4,5]. The overvoltage in motor terminals tends to induce high-frequency resonances in the system and may damage the winding insulation and shorten the lifespan of the motor [6]. This high dv/dt voltage pulse from PWM converters also generates leakage (CM) current, which flows through parasitic capacitance to the motor frame and the ground. In rail vehicle applications, this leakage current may lead to signal failure in the transportation system and safety risk to passengers. An issue with the bearing current, which flows between the rotor shaft and the motor stator frame, is also observed [7,8]. Three factors that contribute to the bearing current are discussed in Refs. [7,8], and one of them is electric discharge machining (EDM) current [9]. The EDM current is caused by the discharging of the parasitic capacitance between the rotor shaft and the motor frame; it damages lubrication in bearings and eventually leads to bearing failure. Furthermore, the severe impact of EMI in actual applications (e.g., railway system) may affect electromechanical systems (winding insulation, bearing and shaft failure, etc.), people and equipment near the rail vehicles (touch potential), and communications in transportation systems (sensors and signal failure, automatic train protection failure, and disturbance on the train radio system) [10–12]. Therefore, European [13] and international standards [14] have been established to regulate the EMI emissions in railway and VFD systems.

Motor modeling, inverter modeling, and EMI noise suppression in VFD systems have been extensively studied for the past 20 years due to the complexity and significance of EMI issues in VFD systems. This article reviews high-frequency EMI models of the sub-modules in VFD systems, such as AC motors, bearings, and rectifier-inverters, and then proceeds to evaluate AC motor models in terms of model structure, component parameterization, applied frequency range, and model accuracy against measured results. In terms of model structures and physical meanings, high-frequency motor models are categorized into three groups: Physical models [15–18], behavior models [19–37], and transmission line and T models [38]. Parameters are generally extracted and determined through trial and error based on measurements, optimized algorithm based on measurements, and parameterization done in accordance with motor geometry. In actual applications (e.g., rail vehicles), long cables between the inverter and the motor affect the high-frequency impedance characteristics of the system. This phenomenon has been studied in Refs. [25,26,36,39,40]. As mentioned above, harmful bearing current shortens the lifespan of motor bearings. Bearing models, EDM current reduction, and relevant issues have been discussed in Refs. [7–9,16,34,41–52]. The rectifier-inverters play a major role as EMI noise sources in VFD systems, because they generate high dv/dt voltage waveforms. In EMI propagation analysis, conventional two-level rectifiers or inverters have been represented with a CM voltage source [53,54].

Several techniques for EMI noise suppression, which aim to eliminate EMI noise and keep the noise level within the EMI standards in VFD systems [13,14], are reviewed and evaluated. Three different techniques are commonly applied in EMI noise reduction: EMI noise suppression with passive components [55–70], EMI noise suppression with active components [71–81], and CM voltage source suppression with optimized modulation [82–94]. EMI noise suppression techniques with passive components include passive filter and Wheatstone bridge balance techniques. Passive components in motor drive systems are bulky (considering the voltage and current levels) and suffer from parasitic effects [95], resulting in the unsatisfactory performance of passive component suppression techniques. Active filters that are applied to VFD systems for noise reduction sense the noise current or voltage, and then inject a current or voltage with opposite polarity but the same magnitude into the circuit to cancel the EMI noise. The first two techniques are integrated to form a hybrid filter technique [75]. Apart from the abovementioned noise suppression methods, CM voltage noise source reduction techniques that involve neither passive nor active components are also summarized. These techniques reduce CM voltage noise sources by modulating the switching states in a control scheme. However, certain conditions should be met before applying these techniques.

The rest of the paper is divided into sections. The existing AC motor modeling and parameterization techniques are reviewed in Section 2. The models are classified in this section, and their advantages and disadvantages are also discussed. In Section 3, bearing models are evaluated and bearing current reduction techniques are summarized. The conventional rectifier-inverter motor drive system modeling and circuit analysis techniques for EMI noise modeling are discussed in Section 4. EMI noise suppression techniques, including passive filter, Wheatstone bridge balance, active filter, and optimized modulation techniques, are reviewed and evaluated based on the developed models in Section 5.

2 AC motor modeling for EMI analysis

2.1 Measurement setup for the high-frequency impedance of an AC motor

Most AC motor modeling and parameterization methods for high-frequency components are based on the measured results of the motor impedance. The magnitude and phase of CM and differential-mode (DM) impedances are measured as functions of frequency (Fig. 4). As can be seen, CM current flows from CM noise sources to three-phase windings and then flows back to the source at the grounding path. DM current represents the high-frequency components flowing in between the phases. The objective of AC motor EMI modeling is to match both CM and DM impedances in the concerned frequency range against the measurement. These EMI models are discussed in later sections.

2.2 High-frequency models for AC motors

Generally, the motor models discussed in the literature are categorized into three groups (Fig. 5): Physical models, behavior models, and transmission line and T models. Physical models focus on impedance over a wide frequency range. Such models start from the low-frequency model of the motor (e.g., T model or d-q model), which represents the electromechanical performance of the motor. By adding parasitic parameters (e.g., winding stray capacitance, winding to frame stray capacitance), these models describe the high-frequency characteristics of the motor at the same time. However, due to the complex physical structures of AC motors and the parasitic coupling effects within motors, physical models do not have accurate impedance prediction capabilities in high-frequency ranges, especially in high-frequency resonances. Compared with the physical model, behavior models are more accurate in high-frequency ranges but lack information on the low-frequency electromechanical characteristics of the motor. Various topologies are introduced in this model to fit the measured results.

Two types of behavior models are reviewed in this paper. Circuit-based behavior models use different circuits (multi-stage resistor-inductor-capacitor (RLC) networks and simplified lumped circuits) to match the impedance curves of the measured CM and DM impedances. Non-circuit-based models use frequency functions to fit the measured impedance curves. Multi-stage RLC circuits accurately match the measured high-frequency results of AC motors, because such circuits provide detailed resonance peaks and valleys in high-frequency impedance curves. However, determining the component parameters in a multi-stage RLC model is difficult and complicated. Therefore, the lumped model, a simplified circuit that describes the measured impedance curves, is adopted to replace the multi-stage RLC model. Compared with the multi-stage RLC circuit model, the lumped model has an easier parameterization process; however, it is less accurate. Another behavior model is based on the curve-fitting of the frequency function matrix. A recently proposed comprehensive model integrates physical and high-frequency transmission line models, and is compatible with most of the abovementioned models. The comparison of the said models is illustrated in another section.

Physical models. In an induction motor, the rotor circuit is physically isolated from that of the stator. The T equivalent circuit, shown in Fig. 6(a), is adopted to simplify the complicated relationship between the stator and rotor circuits; this is achieved by referring the rotor-side electromechanical quantities to the stator side. This structure is defined in Ref. [96] and is used for low-

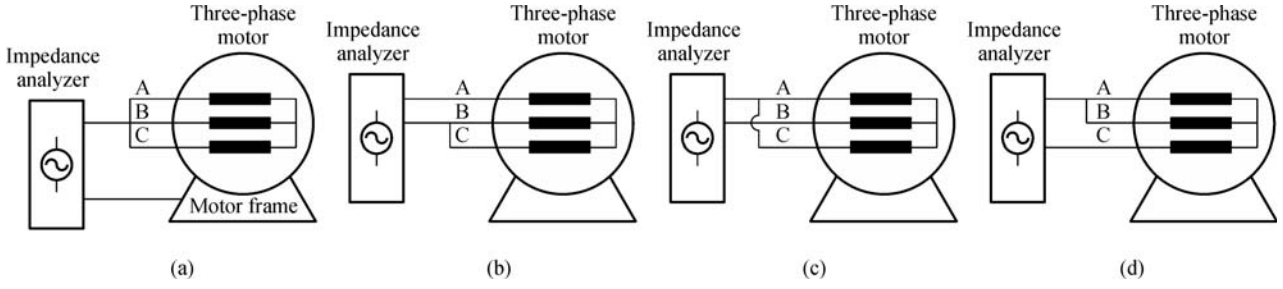

Fig. 4 Impedance measurement setup. (a) CM impedance; (b) Phase A DM impedance; (c) Phase B DM impedance; (d) Phase C DM impedance

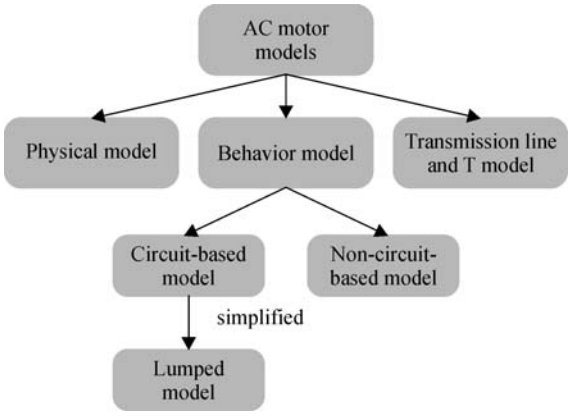

Fig. 5 Classification of EMI models for motors, as presented in the literature

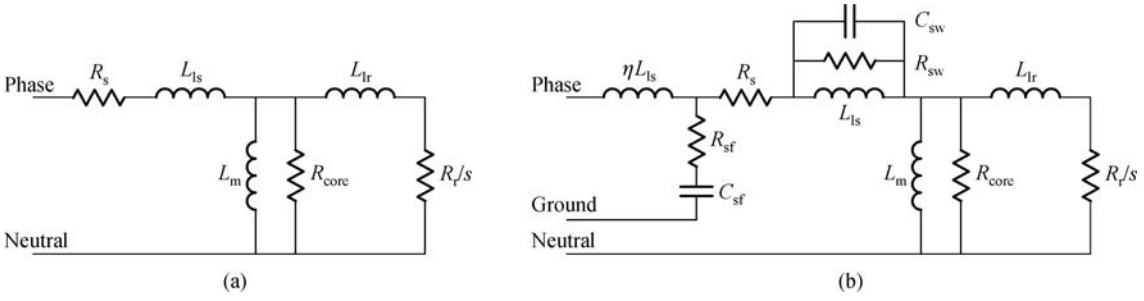

Fig. 6 Proposed motor model in Refs. [16,17]. (a) T model; (b) proposed single-phase physical model

frequency parameterization. In considering the high-frequency parasitic effects in stator windings [16,17], researchers have proposed a new phase model based on the T equivalent circuit, in which R_{sf} and C_{sf} represent the coupling path from the stator winding to the stator frame, and C_{sw} and R_{sw} represent the equivalent parallel capacitance and equivalent winding and core loss of the stator winding. This model shows a wide frequency matching range with the measured results from dozens of Hz to10 MHz. However, the model cannot fit the measured results in the mid-frequency range (10–300 kHz), because it neglects the magnetic coupling effects in-between phases. The accuracy of the model is improved when the coupling effects on magnetic inductance L_m are considered. A physical model proposed in Ref. [15] is based on a low-frequency d-q model that is parallel with high-frequency parasitic parameters. This model is applied to a narrower frequency range (1 kHz–2 MHz) than those employed in previous models [16,17]. The physical model introduced in Refs. [16,17] not only predicts the EMI characteristics of the motor, but also monitors motor health at a standstill state [18]. The failure is identified by comparing the impedance curves of the originally healthy motor with the motor with possible damages, because failures (e.g., liquid intrusion, burnout, insulation breakdown) tend to influence the structure of the model in Fig. 6(b) and the parameters of the model, such as capacitances C_{sf} and C_{sw}.

Behavior models. Behavior models are widely adopted in the analysis of high-frequency motors because of their accuracy in the concerned EMI frequency ranges. Behavior models are categorized as circuit-based and non-circuit-based models according to the impedance curve-fitting method. For non-circuit-based behavior models [22,28], a curve-fitting matrix in Fig. 7 is adopted to store the magnitude and phase information of the CM and DM impedances of the motor. This matrix is a function of frequency and is described by the curve-fitting method. This non-circuit-based model achieves good matching with the measured results, because it directly transfers the measured information into the frequency function matrix. However, information on the motor's structural optimization for EMI noise reduction is difficult to provide because this model has no physical meaning.

Circuit-based models aim to find an equivalent circuit to fit the measured impedance and phase information of the motor. Such a circuit does not necessarily include the physical meaning of the motor. The phase-belt circuit (Fig. 8) is the unit circuit used in multi-stage RLC models. However, circuit-based model has no fixed phase-belt circuits, because no unique circuit matches the different measured impedance curves. The authors consider the

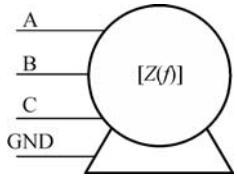

Fig. 7 Non-circuit-based behavior model

high-frequency characteristics of the motor in the phase-belt circuit as a combination of several RLC circuit units [19–21,24,27,29], as shown in Fig. 9. Behavior models have significantly more components than physical models. The parameterization process is further complicated by the coupling effects in each phase and among three phases. The extraction method for the parameters are detailed in a later section in this paper. Apart from the phase-belt model, a multi-stage π model (Fig. 10) is also adopted in fitting the high-frequency impedance of the motor [23,25]. Generally, this circuit-based model has good impedance matching compared with physical models; however, parameter extraction is more complicated.

The lumped model is adopted in fitting the measured impedance curves to simplify the parameterization process. The π model proposed in Ref. [32] is shown in Fig. 11(a). In Fig. 11(a), R_e and R_{cu} represent the iron and copper loss in the stator, and L_{str} and L_M represent the leakage inductance and magnetic inductance in each phase, respectively. Branches C_{g1} and R_{g1} represent the path from the motor terminals to the stator frame parasitic parameters, and C_{g2} and R_{g2} represent the path from the neutral to the stator frame parasitic parameters. However, the impedance curve does not match the measured results well due to the limited number of components in the lumped model. Therefore, the authors have to revise the π model by adding C_{ad} and R_{ad} to fit the details in the measured curves (multiple resonance peaks and valleys) in Fig. 11(b).

Transmission line and T model [38]. The above-mentioned physical models reflect the load effects in low-frequency ranges because they use the T model of the AC motor. The benefit of utilizing the T model in EMI modeling is that the efficient frequency range is expanded to include frequencies as low as dozens of Hz; moreover, this model considers the influence of the rotor and the load on the motor model. However, the high-frequency parasitic parameters in physical models [16,17] include the lumped capacitance, inductance, and resistance, and the accuracy of physical models is limited in the mid- and high-frequency ranges. In EMI frequency ranges, the motor's stator winding length and the length of the long cables between the inverter and the motor are comparable with the wavelength. Therefore, mid- and high-frequency impedance performance can be described with the transmission

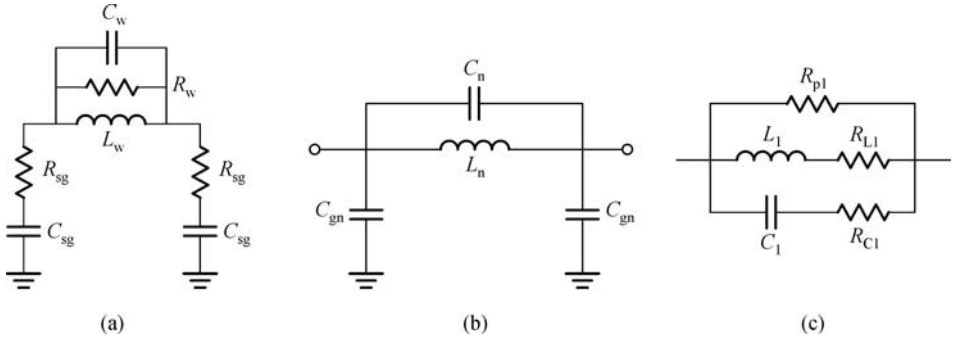

Fig. 8 Phase-belt circuits discussed in Refs. [19–21]

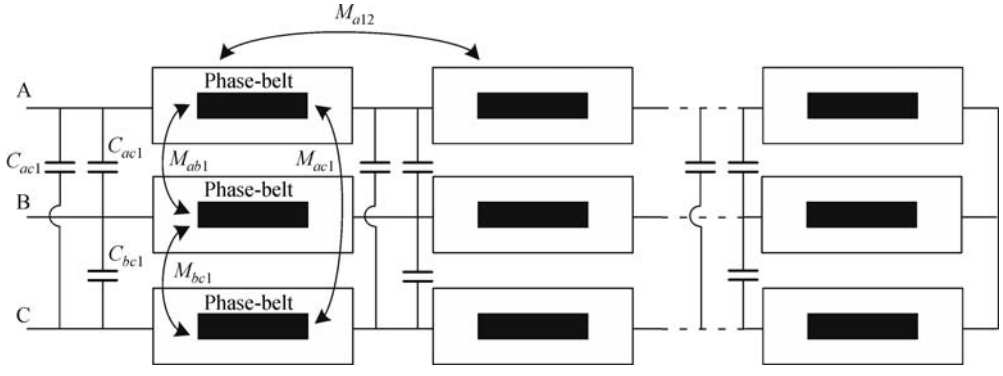

Fig. 9 General topology of a multi-stage RLC model

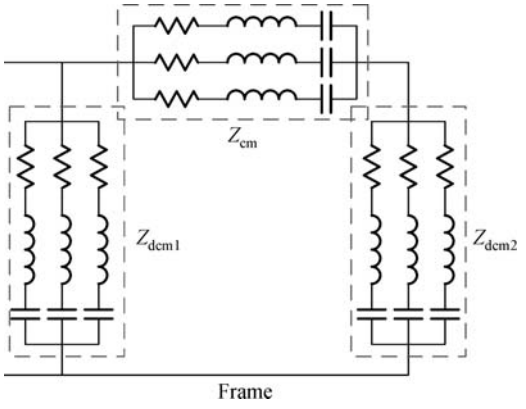

Fig. 10 Multi-stage π model in Refs. [23,25]

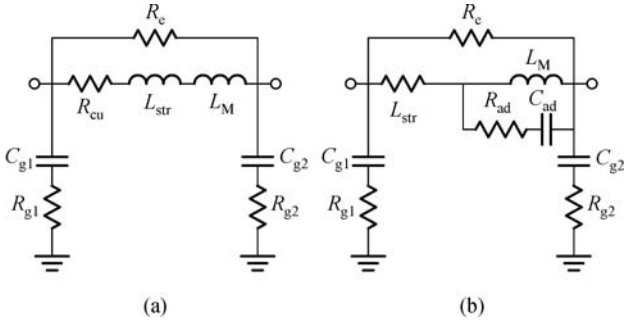

Fig. 11 Lumped model in Ref. [32]

line model in Fig. 12. However, parameterization is complicated in the transmission line model, and an optimized algorithm must be adopted to determine the value of the component. A comprehensive three-phase AC motor EMI model is developed by combining the transmission line model (high-frequency) and T model (low-frequency) together, as shown in Fig. 13. The resulting model matches the measured impedance curves in a wide frequency range and achieves accuracy in the concerned frequency range.

2.3 Parameterization of the high-frequency models

The parameterization of the motor model components is important in ensuring the accuracy of the proposed model. This process can be done in three main ways: 1) Parameterization based on motor geometry, 2) parameterization with trial and error, and 3) parameterization with an optimized algorithm, which has been proposed recently [38]. The optimized algorithm is the most accurate among all the methods. Another advantage is that the optimization technique utilizes all the measured impedances and only needs a small amount of human interference. For example, the trial-and-error process can be eliminated by selecting several typical points from the measured impedance curve. Therefore, parameterization is considerably simpler and faster than all the other methods. The approximate (trial and error) calculation method is a commonly adopted technique for the parameterization of high-frequency motor models. The calculation procedure is largely related to the circuit model, and this procedure can be simplified with a one-stage model that has low accuracy and can be complicated with a multi-stage RLC model. Parameterization techniques based on motor geometry and finite element analysis are not frequently used because of their inaccuracy and considerable time requirement.

Parameterization with trial-and-error method. This technique is widely adopted in behavior model parameterization for both the multi-stage RLC and lumped models. This method identifies the resonance peaks and valleys in the DM and CM measurement impedance curves of the AC motor. On the basis of the equivalent DM and CM circuits of the proposed model, the researchers attempt to find the R, L, and C values for the selected resonance peaks and valleys in the measured impedance curves. For example, the equivalent DM and CM circuits of a multi-stage model, as proposed in Ref. [29], are shown in Fig. 14. As can be seen in the figure, the parameterization of this multi-stage RLC circuit is complicated; hence, an assumption (1) must be made to simplify it. With an assumption at each DM or

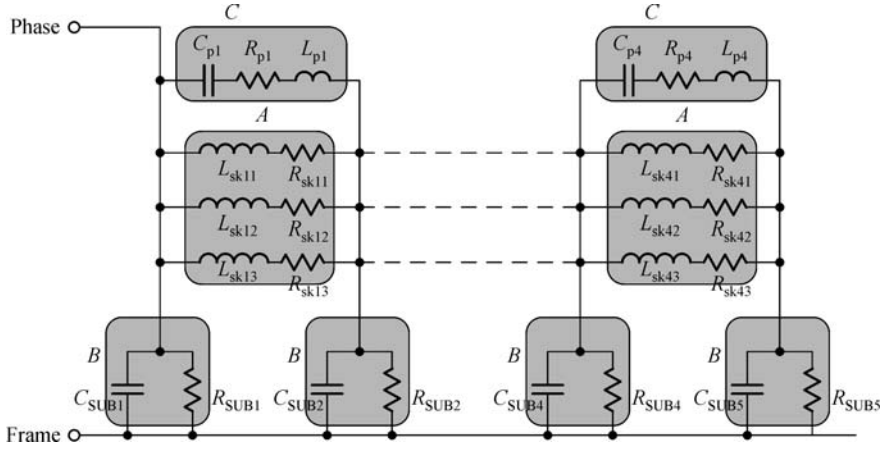

Fig. 12 Long cable and stator winding transmission line model in a high-frequency range

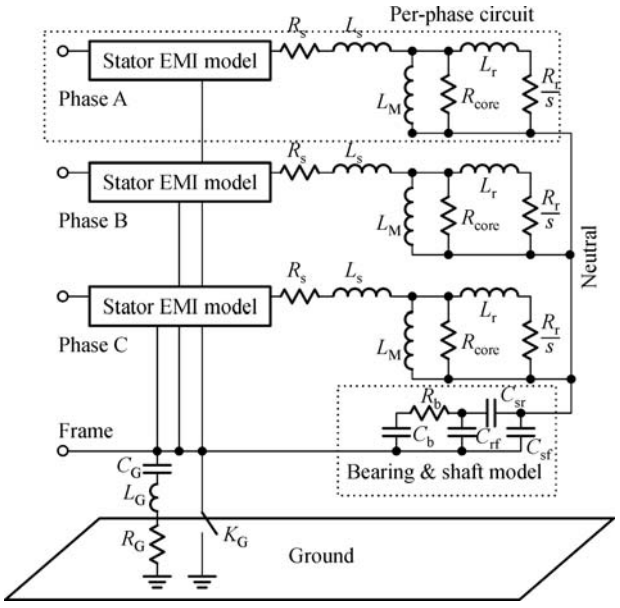

Fig. 13 Three-phase EMI model in Ref. [38]

CM resonance peak in the measured impedance curves, the circuit is simplified as a one-stage RLC circuit, and the parameters are determined by combining CM and DM circuits [29]. Parameterization in a lumped circuit model is considerably easier than that in a multi-stage model because the former has less components. However, accuracy is limited in a simplified model.

$$\begin{matrix} L_{D1}<<L_{D2}<<...<<L_{Dn} \\ L_{C1}<<L_{C2}<<...<<L_{Cn} \end{matrix}. \quad (1)$$

Parameterization based on motor geometry. Another way to extract parasitic parameters is by performing calculation based on the physical geometry of a motor. The slot effect is considered in the parameterization of the parasitic capacitance in an AC motor in Ref. [16]. The capacitance from the stator winding to the stator frame in one slot is estimated in Fig. 15. Three capacitances are included: Stator winding-to-slot inner wall capacitance (winding insulation d_1), slot inner wall-to-outer wall capacitance (slot insulation d_2), and the capacitance due to possible random small air gaps between the slot line and the frame (d_3). Moreover, the slot is approximated to be rectangular in shape. However, the calculated capacitance still requires correction factors to match the real case. The selection of correction factors may vary across different motor types, and a generalized guideline based on motor geometry is missed. Another method, which uses finite element analysis modeling with motor geometry, has been introduced in Ref. [24]. In 3D electromagnetic field analysis, the stray capacitance is calculated with static electric field analysis, and the inductance and resistance of the stator winding are evaluated with magnetic field analysis. An equivalent circuit model for the AC motor is proposed in Ref. [24]. The impedance magnitude and phase match the measured results better than the calculated results reported in Ref. [16]. However, this finite element analysis (FEA) method is time consuming because it requires significant 3D modeling with a software.

Parameterization using an optimized algorithm. Parameterization in a multi-stage RLC circuit EMI motor model is complicated and even impossible to carry out via trial and error or calculation. Thus, an optimized algorithm is often adopted to solve complicated model parameterization problems in motor modeling. Furthermore, accuracy is better with an optimized algorithm than with the trial-and-error method. For example, a behavior model has been proposed in Ref. [38] based on the measured impedance curves. This model combines the low-frequency T model of the motor shown in Fig. 16(a), and the high-frequency behavior model of the long cable and stator windings shown in Fig. 16(b). The parameterization of the four-stage RLC circuit is further complicated by the respective resonance peaks and valleys of the measured impedance curves. Although the values of RLC can be obtained based on measured resonance peaks and valleys at several operating points, all the other operating points in the concerned frequency range cannot guarantee a good match. It is shown in Fig. 17 that the flowchart of the optimized algorithm applied in Ref. [38]. First, the error between the predicted value and the source value (measured impedance) is defined before the iteration. Then, the objective function is selected based on the error in MATLAB. Iteration is conducted with the selected objective function. Each operating point of the measured impedance is evaluated, and the parameters are selected such that the difference between predicted results and measured results within the errors is set at the beginning. This method is advantageous because of its accuracy in all measured operating points; hence, trial and error is avoided. However, running iterations to achieve a small amount of errors can be time consuming, and the obtained RLC values may be out of physical meanings.

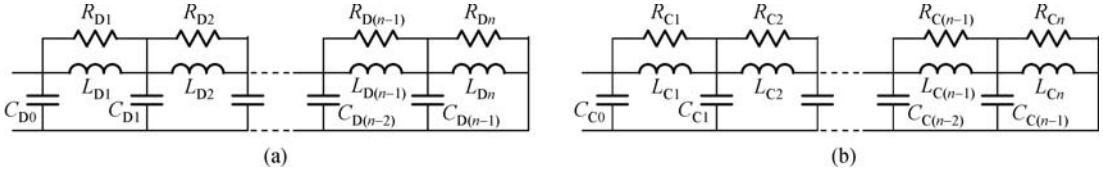

Fig. 14 RLC model. (a) Equivalent DM circuit; (b) CM circuit in Ref. [29]

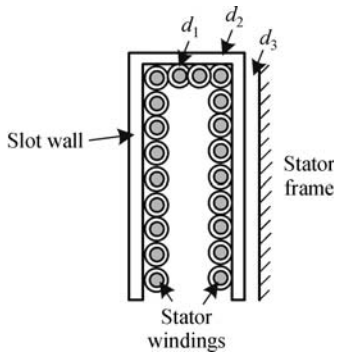

Fig. 15 Equivalent physical structure of a stator slot

This section presents a summary of the different AC motor models. Although physical models retain the low-frequency performance of the electromechanical system of the AC motor, applying them to other motor systems is challenging due to their parameterization inaccuracy and the unclear definition of the equations that are used to extract the parasitic parameters. In addition, these physical models are not effective and accurate when the effects of long cables are considered. Compared with physical models, multi-stage RLC models match motor DM and CM impedances more accurately because they commonly comprise several RLC segments, which match the resonance peaks and valleys in the measured results. However, these models are a circuit "solution" to the measured results, and they vary across different papers. Thus, obtaining a general idea on AC motor modeling is difficult, and solutions may vary even for the same motor. Furthermore, its characteristics are difficult to identify in EMI analysis because it lacks physical meanings. The advantage of multi-stage RLC models is that they consider the long cable effect together with the motor. Due to the complicated parameterization in multi-stage RLC models, a simplified lumped model is thus proposed to match the impedance curves when they have less resonance peaks and valleys. Parameterization, which is usually employed in this method, is easier in the π model than in a multi-stage RLC model. However, the π model also has no physical meanings, and neither load effects in the low-frequency range nor long cable effects in the EMI frequency range is available in this model. Hence, long cable modeling should be considered in the EMI modeling of drive systems if motor modeling is based only on short cable cases. The transmission line [36] (lossy and lossless) and ladder models [39,40] are commonly adopted in long cable modeling. Meanwhile, a matrix-based behavior model is proposed based on the curve-fitting of the measured results. Although this model can achieve a good match, it cannot be applied to circuit simulation and lacks physical meaning. Finally, a comprehensive circuit that includes transmission line and T models is proposed. This circuit not only retains the low-frequency load characteristics in AC motors but also matches the high-frequency impedance curves and long cable effects in transmission line circuits. Based on this model, the applied frequency range is expanded and both impedance magnitude and phase are matched more accurately.

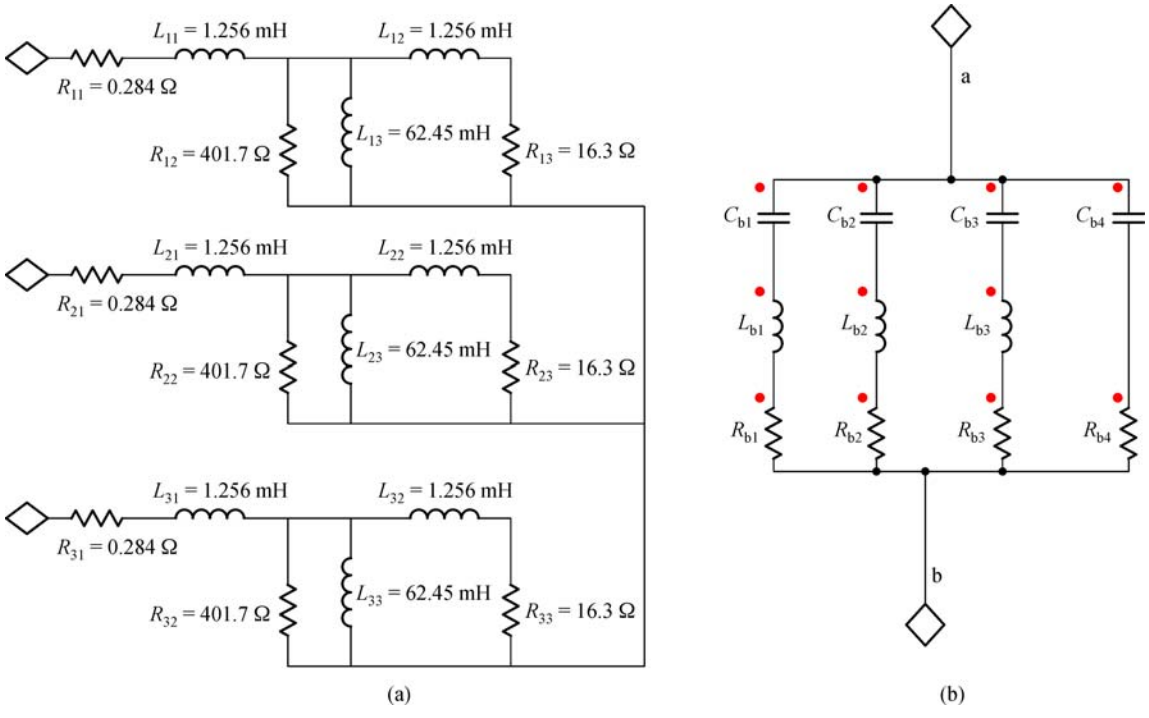

Fig. 16 (a) T model; (b) high-frequency behavior model in Ref. [38]

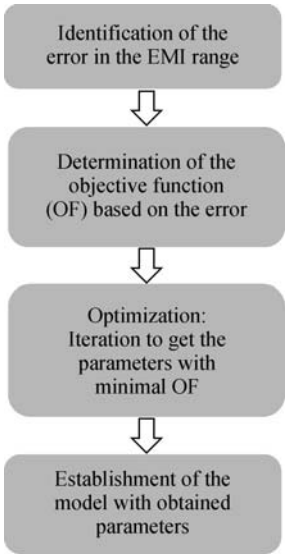

Fig. 17 Flowchart of the optimized algorithm in Ref. [38]

3 Motor bearing modeling and EDM current reduction

Bearing may conduct CM currents due to the coupling effects in electrical machines. However, the coupling current from the stator winding to the rotor side is always ignored in most EMI noise propagation analyses, because the magnitude of CM currents that flow from the stator winding to the rotor is smaller than that of the CM currents flowing from the stator winding to the stator frame.

However, bearing modeling has been discussed in many studies because bearing currents or shaft currents can damage motor bearings and shorten the lifespan of motor drives. Bearing currents and their sources have been measured and identified in Refs. [7,8]. Three types of bearing currents are discussed in those studies: 1) Discharging current of the voltage on the stator-rotor parasitic capacitance (EDM current), 2) CM current due to the coupling path between the stator winding and the rotor, and 3) circulating bearing current due to the time-varying magnetic flux encircling in the motor shaft. Among the three, the EDM current has the current spikes that flow through the bearings' lubricating liquid and can damage the bearings.

3.1 Bearing models for AC motors

A bearing capacitance calculation is discussed in Ref. [48], and the equations are given based on the motor and bearing geometry in Fig. 18. Capacitances C_{b1} and C_{b2} are formed when a motor operates at a high speed, and are charged by the CM currents from the stator windings. However, the capacitance is broken down under certain conditions, and as a result, large discharging current spikes damage the lubricating liquid in motor bearings. Roller and ball bearing capacitances has been analyzed with the finite element method in Ref. [49]. In the verification of the simulation and measurement, the detailed model shows a good match in time domain waveforms.

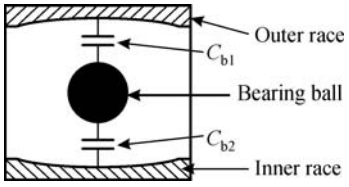

Fig. 18 Physical structure of the bearing

A simplified bearing model has been introduced in Ref. [41] to simulate the bearing current spike and shaft voltage resonance in time domain. In Ref. [43], a revised bearing and motor circuit model, shown in Fig. 19, has been proposed to analyze the high-frequency noise current flowing in the motor shaft and bearing. As can be seen, C_{sf} is the parasitic capacitance between the stator winding and the stator frame, C_{sr} is the capacitance between the stator winding and the rotor, C_{rf} is the capacitance between the rotor and the stator frame, C_b is the capacitance between the bearing and the stator frame, and Z_b simulates the mechanism when the bearing is well-conducted or otherwise. Several mitigation methods are discussed in this paper based on the understanding of the coupling path in the circuit. These mitigation methods include reducing the CM voltage, reducing the coupling from motor stator winding to rotor, connecting the shaft with ground, and redesigning the CM propagation circuitry. In Refs. [34,52], the bearing model has been verified in time-domain analysis. In Ref. [33], four capacitances (i.e., the stator winding to rotor capacitance, the stator frame to rotor capacitance, the drive-end bearing capacitance, and non-drive-end bearing capacitance) have been analyzed with a capacitive voltage divider, and then verified in a time-domain shaft voltage and bearing current measurement.

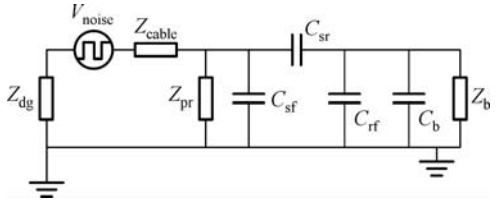

Fig. 19 Bearing model proposed in Ref. [43]

The shaft end-to-end voltage, which represents the voltage difference between two ends of the rotor shaft, has been discussed in Refs. [50,51] and several causes have been identified. First, the CM voltage causes dielectric breakdown of lubricating liquid films in one bearing, while maintaining their dielectric insulation in the other bearing. Second, the CM current in the three-phase stator windings

generates a time-varying magnetic flux surrounding the rotor shaft. This magnetic flux induces shaft end-to-end voltage. Third, the asymmetrical parasitic capacitance between the stator windings and the motor frame, and the asymmetrical inductance in the coils cause a differential-mode current flowing through the shaft in axial direction. This current generates the shaft end-to-end voltage.

3.2 Bearing current reduction techniques

With the discussion of the mechanisms leading to shaft voltage and bearing current in AC motor drive systems, various reduction methods have also been introduced [43,45]. First, the bearing current and shaft voltage are suppressed by reducing the CM voltage magnitude at the noise source side. For example, with the optimized space vector pulse width modulation (SVPWM), the CM voltage can be reduced compared with the conventional SVPWM. Second, reducing the coupling from the motor stator winding to the rotor can also suppress the bearing current and shaft voltage to increase the capacitance between the winding and the frame, thus reducing the capacitance between the stator winding and the rotor. Hence, most of the CM current will flow from the winding to the frame instead of flowing to the rotor. The third method is reducing the shaft voltage to connect the rotor shaft directly to the ground, but this requires extra components, such as a grounding brush to bypass the shaft current from the rotor to the ground. Finally, the bearing current and shaft voltage can be suppressed based on the equivalent CM circuit in motor drive systems. For example, grounding the neutral point of the Y-connected stator windings, increasing the propagation impedance with EMI filters, and replacing the conventional bearings with dielectric ceramic bearings can reduce the bearing current and shaft voltage.

4 EMI source modeling for VFD systems

Rectifier-inverter systems are widely used in motor drive systems. The switching rectifiers and inverters behave like a noise source in motor drive systems. The input AC/DC rectifier can either be an uncontrollable diode bridge or a controllable active rectifier. Past studies [53,54,59,60] presented a basic understanding on how the system is modeled in a rectifier-inverter motor drive system.

4.1 EMI modeling for rectifiers and inverters in motor drive systems

As shown in Fig. 20, a typical three-phase motor drive system consists of the three-phase power input, the main transformer, the AC-DC uncontrollable diode bridge rectifier, a 2-level inverter, and a three-phase motor. The heatsink of the AC-DC-AC converter is directly connected to the ground for safety considerations. The equivalent CM circuit in a front-end rectifier-inverter system with input diode bridge in Refs. [59,60] is shown in Fig. 21(a). The diode bridge and inverter can be replaced by CM voltage sources. Two voltage sources are placed in a series, and the parasitic capacitance of the semiconductors and the DC bus are considered. The CM voltage source has a frequency equals to thrice that of the grid frequency in a three-phase system and twice that in a single-phase system. As for the CM voltage source due to the 2-level inverter, the frequency of this voltage source could be very high because of high switching frequency. Here, $3C_{\text{diode}}$ represents the parasitic capacitance between the AC terminals of the diode bridge and the ground, C_{bus} represents the parasitic capacitance between the DC bus and the ground, and $3C_{\text{inverter}}$ represents the parasitic capacitance between AC terminals of the inverter and the ground. Given that the diode bridge's equivalent CM voltage source only generates the third-order of grid fundamental frequency harmonics and has little influence on EMI equivalent circuits, the diode rectifier can thus be ignored in the EMI analysis shown in Fig. 21(b).

In an active rectifier-inverter motor drive system [53], shown in Fig. 22, the diode bridge is replaced by an active switching rectifier. With a higher frequency than the grid

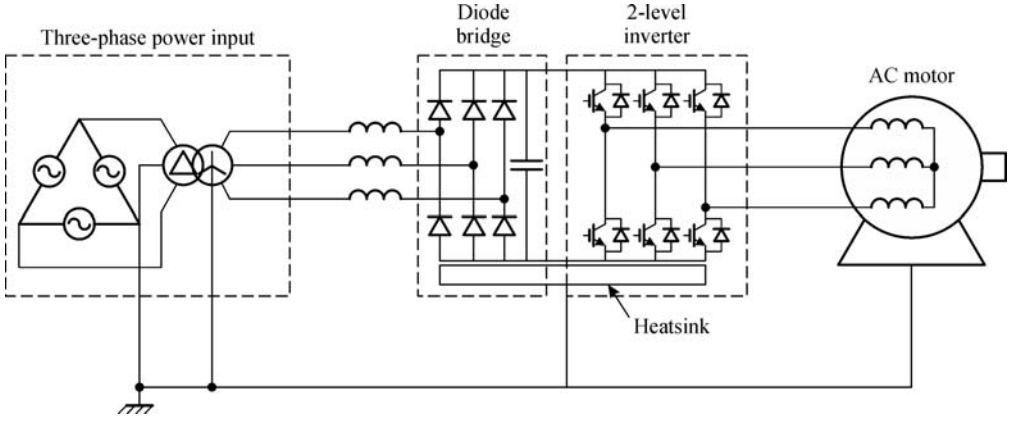

Fig. 20 A diode bridge-inverter motor drive system in Refs. [59,60]

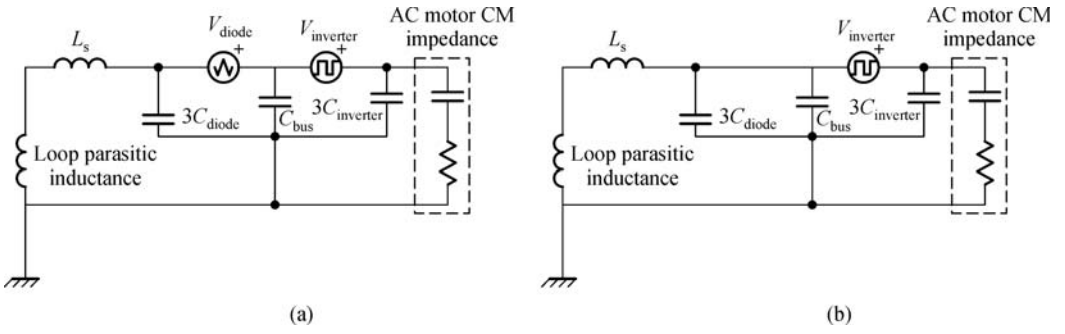

Fig. 21 CM noise equivalent circuits. (a) Equivalent CM circuit; (b) simplified CM circuit

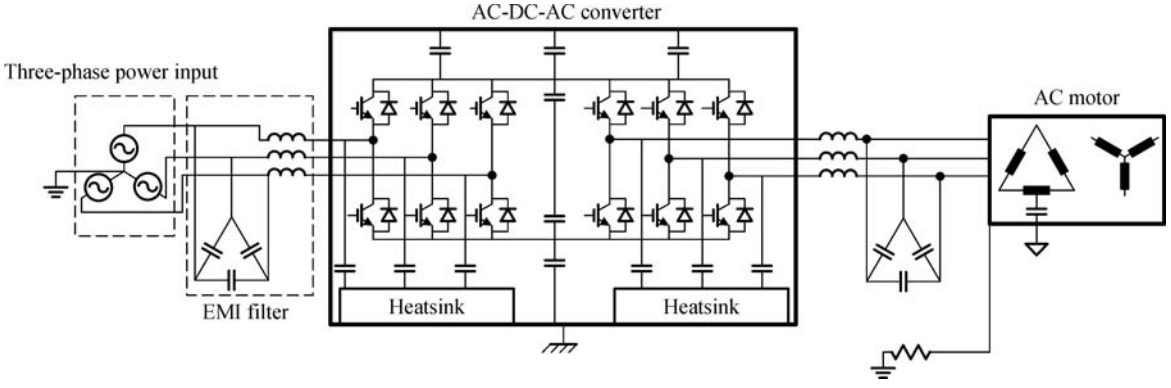

Fig. 22 An active rectifier-inverter motor drive system in Ref. [53]

frequency due to its high switching frequency, the equivalent CM voltage source of this rectifier cannot be ignored in CM circuit analysis, as shown in Fig. 23. Here, V_{rec} and V_{inv} are the equivalent CM voltage sources of the active rectifier and the 2-level inverter, respectively. The parasitic capacitance of the rectifier, DC bus, and inverter are represented by $3C_{rec}$, C_{bus}, and $3C_{inv}$, respectively. Apart from conventional converter EMI modeling, the EMI modeling of a neutral clamped converter (NPC) system has been introduced in Ref. [97].

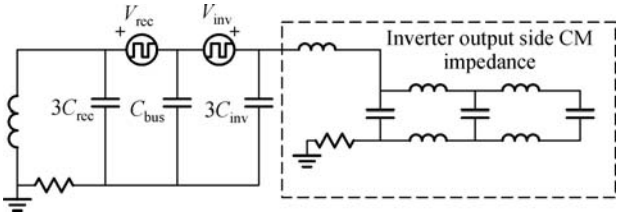

Fig. 23 Equivalent CM circuit in Ref. [53]

4.2 Techniques for the analysis of multi-source EMI models

As previously discussed, the equivalent CM circuit in a diode bridge-inverter motor drive system can be simplified as a single voltage source system. However, in an active rectifier-inverter motor drive system, or in other complicated AC-DC-AC converter systems with more than one equivalent voltage sources, the circuit analysis techniques can be adopted to simplify the CM models.

Superposition theory is valid for multi-source linear system analysis (Fig. 23). As shown in Fig. 24, the two-voltage-source system can be divided into two single-source systems. The noise current/voltage is analyzed

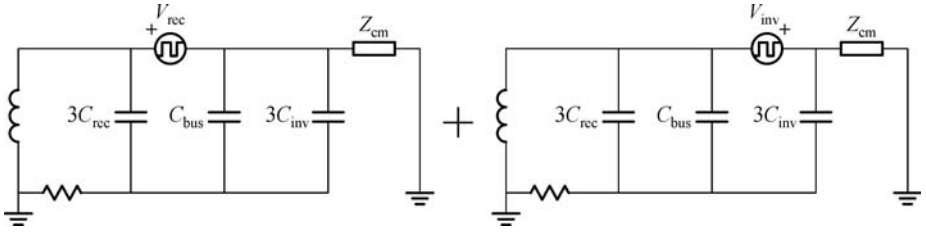

Fig. 24 Superposition theory used in EMI analysis

separately in each circuit, and the total noise current/voltage is the sum of the noise current/voltage of the two single-source systems.

In the active rectifier-inverter motor drive system presented in Ref. [54] and in Fig. 25, a different technique can be adopted to convert the double-source system into a single-source system. Figure 26 shows a more direct way to model the system with Thevenin's theorem. Two voltage sources V_{rec}, V_{inv}, and their respective source impedances, Z_{cf} and Z_{Lf}, are replaced by an equivalent voltage source V_{th} and an equivalent source impedance Z_{th}. CM noise reduction techniques can be directly applied to this equivalent circuit.

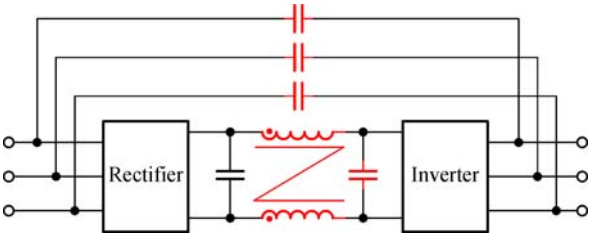

Fig. 25 An active rectifier-inverter system in Ref. [54]

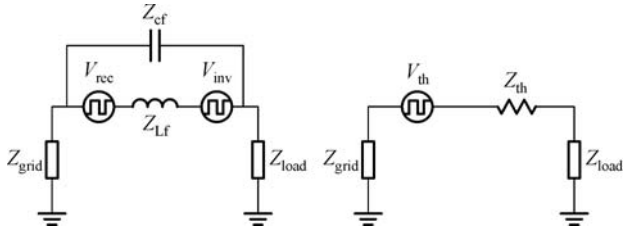

Fig. 26 The Thevenin's theorem in EMI analysis

5 EMI suppression techniques in VFD systems

Following the modeling techniques in motor drive systems, the noise suppression techniques can be applied to reduce the high frequency noise. Four techniques are reviewed in the following sections: Passive filters, Wheatstone bridge balance techniques, active filters, and optimized modulation techniques (Fig. 27). Their corresponding mechanisms will be illustrated later.

Conventionally, passive components have been widely adopted in the suppression of EMI noises, because doing so is less complicated and easier for the designers [45,55–60,62,63,66,68–70,98,99]. However, the parasitic parameters of the passive filter can greatly degrade the high frequency performance of the filter [100]. In addition, the resonances of the parasitic parameters at high frequencies could generate noise peaks in the frequency spectrum as well as exceed standard limits. In order to reduce the size of passive filters, active filters are introduced in Refs. [71–81]. Compared with passive filter suppression, the active filter suppression can achieve a smaller size and better high frequency performance, although active switches or amplifiers must first be adopted in the active filters. However, these increase the complexity of the design apart from the design considerations of system reliability and stability. The passive and active filter techniques focus on noise suppression on the EMI propagation path in order to bypass the noise current to the noise source. The third technique concentrates on the noise source reduction based on optimized modulation in rectifiers and inverters [82–94,98]. Different modulation strategies can be used for rectifier and inverter control, in order to reduce CM noise sources.

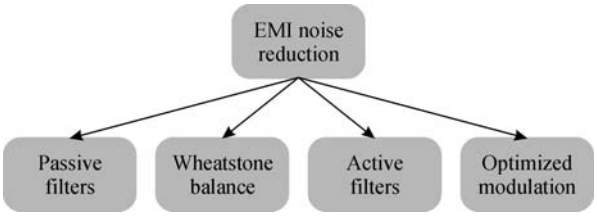

Fig. 27 Classification of EMI noise reduction techniques

5.1 EMI noise suppression with passive filters

A past study [55] proposed two types of suppression circuits: Potential-type suppression and current-type suppression. Potential-type suppression circuit, shown in Fig. 28(a), is usually located between the inverter and the motor. Four coils are coupled on a magnetic core and all the coils have same number of turns. Three coils are placed in a series with three phase currents, and the neutral potential is constructed with a star connected resistor-capacitor (RC) circuit. The fourth coil is connected between the neutral point and the ground or the neutral of the motor. Based on the transformer theory, the CM voltage applied to the three coils then induces a voltage with the same amplitude on the fourth coil to cancel the CM voltage differences between the motor and RC neutral. For the current-type suppression in Fig. 28(b), it is basically the LC filter that provides a high impedance on the CM propagation path with a CM inductor and a low impedance to bypass the CM current with the star-connected capacitors.

In Fig. 28(a), the suppression circuit needs a large resistor and a small capacitor to limit the fundamental frequency current circulating within the RC-star; in turn, this requirement cause power loss and undesired current. In the improved structure shown in Fig. 29 [57], a three-phase coupled iron core inductor is adopted to generate the CM voltage with the star connection. This inductor provides a high impedance across the phase-phase voltage, and it acts like an open circuit for fundamental frequency currents. However, it has a low impedance to the CM currents. The

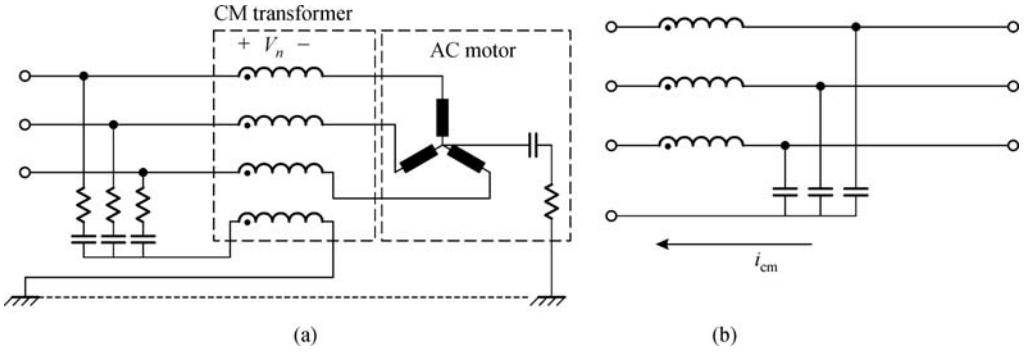

Fig. 28 Passive filters. (a) Potential type suppression; (b) current type suppression in Ref. [55]

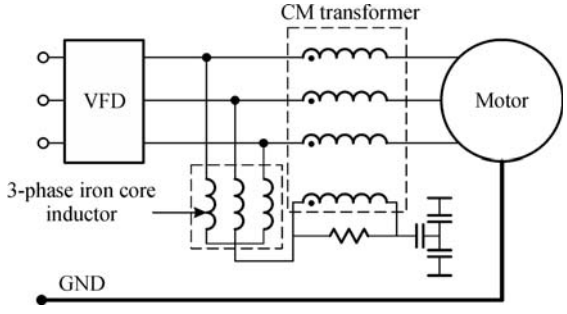

Fig. 29 Potential type suppression with 3-phase iron core inductor

neutral point of this inductor is connected to the fourth coil of the CM transformer, and the other side of the fourth winding is connected to the DC mid-point. Hence, the voltage on the fourth coil of the CM transformer is the same as the CM voltage in this three-phase system. The voltage added to the motor is suppressed by an injected opposite voltage from the CM transformer. In order to block the fundamental frequency current with the 3-phase iron core inductor, the inductance of this inductor should be large; hence, using a bulky inductor in this structure is inevitable. The three-phase balanced inductance must also be achieved and a new type of three-phase coupled inductor with compensation windings has been discussed in Ref. [101].

Past studies [58–60] have investigated a diode bridge-inverter motor drive system, introduced different topologies of the passive filters, and discussed their respective performances. Line impedance stabilization network (LISNs), shown in Fig. 30, are used to measure the CM noise flowing from three-phase system side to the AC grid side. Two EMI filters are inserted into the system to eliminate the CM current flowing through the LISNs.

The CM equivalent circuit of the diode bridge-inverter system is shown in Fig. 31, in which i_{CM} represents the total CM current flowing out of the noise source. By adding R_{cm2} and C_{cm2} branch (a low impedance CM path) between the stator winding neutral point and DC bus mid-point, i_{CM1} can now flow back to source. Given that the parasitic capacitance between the winding and the frame provides a coupling path for CM current i_{GM}, this current flows from the stator windings to the motor frame and to the ground. Part of this current then circulates back to the source through the parasitic capacitance of the converter system, whereas other parts flow to the three-phase AC input. By adding a line EMI filter between the LISNs and the rectifier, the C_{cm} provides a low impedance path for CM current and L_{cm2} provides high impedance to prevent the CM current from flowing through the LISNs. Thus, the CM noise is reduced with passive filters.

Conventionally, the passive filter design can follow the flow chart in Fig. 32. In the figure, Meet Std. represents

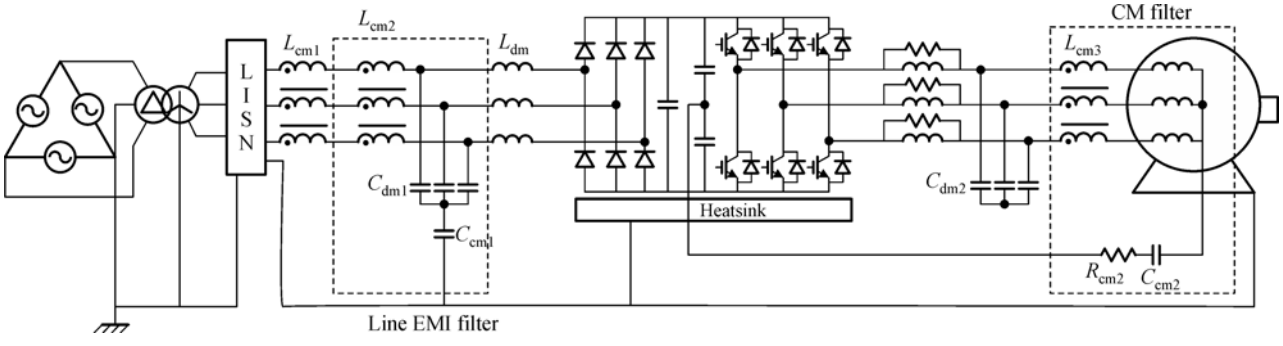

Fig. 30 A diode bridge-inverter motor drive system in Ref. [60]

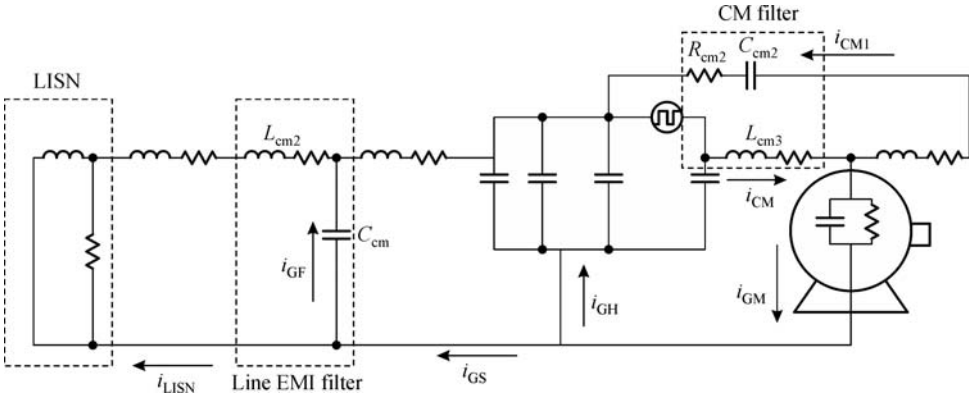

Fig. 31 Equivalent CM circuit in Ref. [60]

whether the measured EMI noise meets the EMI standard. If yes, the system can be considered compatible with EMI standard. Otherwise, low frequency and high frequency noise performance should be checked. If low frequency noise exceeds the EMI standard, a low corner frequency filter should be selected. If high frequency noise exceeds the EMI standard, the performance of the passive components (e.g., inductors and capacitors) needs to be improved. In the passive filter design, the topology of the passive filter is often determined by the impedance mismatch rule with the source and load impedances (Z_S and Z_L) as shown in Fig. 33 [102]. A low-input filter impedance is desired for a high-impedance noise source, and similar to a current source, the low input impedance can reduce the noise voltage added on the EMI filter. For a low-impedance noise source, a high-input filter impedance is desired to limit the noise current in the circuit. This is because the noise source is like a voltage source, and a high-input impedance can reduce noise current flowing through the EMI filter. On the load side, a high-impedance load needs a low output impedance for the filter, given that the noise current from the source side can be bypassed by the low impedance of the filter. Likewise, a low-impedance load needs a high impedance output for the filter, because most of the noise voltage can be dropped on the filter's high output impedance instead of the load. Once the bare noise is measured and the standard is selected, the attenuation requirements can be calculated using Eq. (2) below.

$$V_{\text{bare\_noise}} - V_{\text{std}} = A\text{ttenuation\_req}, \tag{2}$$

where $V_{\text{bare\_noise}}$ represents the measured system's EMI noise without any attenuation techniques, V_{std} represents the EMI limitations which are regulated in the EMI standards. Since they are all in the unit of dBμV, their difference is the required attenuation magnitude (Attenuation_req) in dBμV with the EMI suppression techniques.

The corner frequency of the filter is selected with the theory in Ref. [103]. Other related information is still needed for the parameterization of the RLC values of the passive filter. In Ref. [104], the inductance and capacitance value has been chosen based on maximum current ripple, reactive power limitation, and attenuation requirements. The RLC values can also be determined with an optimized design, such as the minimum filter size design [105]. Then, the noise in the system with the filter is measured to check if it meets the standard. If the noise in the low-frequency range exceeds the standard, a lower corner frequency should be selected to gain a larger attenuation. The possible causes as to why noise in the high-frequency range exceeds the standard and their corresponding solutions are shown in the high-frequency performance check block in Fig. 32. Previous studies have discussed high-frequency parasitic effects and proposed techniques to eliminate the impacts of these effects [106–108]. A past study discussed the interactions between passive filter parasitic components and power interconnects [100], whereas others introduced the damping circuit design [104,109].

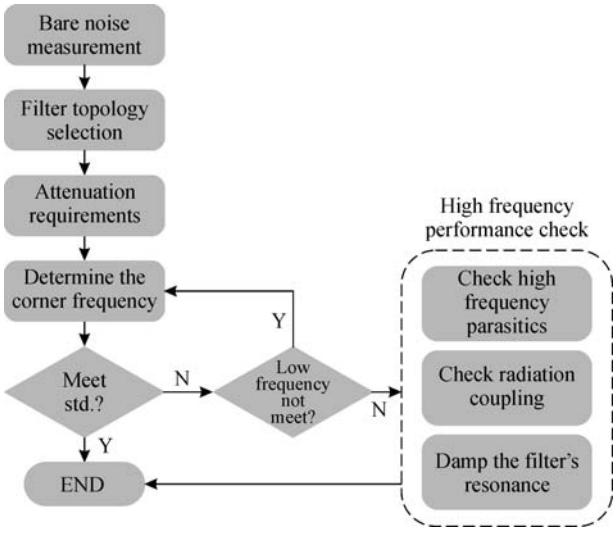

Fig. 32 Passive filter design flow chart

Considering the voltage and current level in motor drive systems, the big capacitors and inductors lead to a very bulky filter design. Several ways to optimize the size, which include the use of three-phase coupled inductors [110–112], inductors integrated with CM and differential-mode inductors [62], and power modules with an integrated CM capacitor [98], have been discussed.

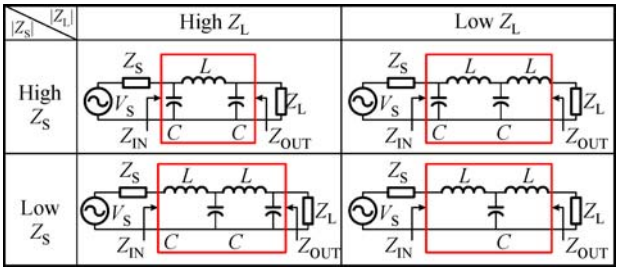

Fig. 33 Topology selection of passive filters based on source and load impedances.

5.2 EMI suppression with Wheatstone balance technique

The Wheatstone bridge balance technique is another way of eliminating the CM noise with passive components. The principle is to construct four impedance branches (R_1, R_2, R_3, and R_4) outside the noise source V_S (Fig. 34). If the ratio of these four branches meets the expression in Eq. (3), the voltage between Points A and B, which is the noise voltage detected by LISNs, becomes zero, as shown in Eq. (4).

$$\frac{R_1}{R_2} = \frac{R_3}{R_4}, \tag{3}$$

$$V_{AB} = \left(\frac{R_2}{R_1 + R_2} - \frac{R_4}{R_3 + R_4}\right) V_S = \left(\frac{1}{\frac{R_1}{R_2} + 1} - \frac{1}{\frac{R_3}{R_4} + 1}\right) V_S. \tag{4}$$

In Ref. [95], the author proposed a Wheatstone bridge balance technique for the single-phase boost PFC converters. This technique can also be applied to a DC-fed motor drive system, as shown in Fig. 35 [64].

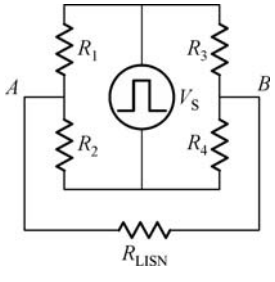

Fig. 34 Wheatstone bridge balance

Here, L_1 is the CM inductor on the DC bus. By adding L_2, which makes $L_1/L_2 = C_{bg}/C_{mg}$, the voltage difference between the output of the Wheatstone bridge is equal to zero, as shown in Fig. 36. Thus, the CM current flowing through the LISNs can be eliminated. The L_2 is selected to guarantee the impedance of the added branch from 150 kHz, with the RLC resonant frequency below 150 kHz. The experimental results show a 15 dB reduction of the CM current at 150 kHz compared with the non-balanced case. However, due to the effects of the parasitic parameters, the technique performance is significantly degraded when the frequency increases. Apart from the Wheatstone bridge balance technique, the parasitic cancellation technique mentioned in Ref. [106] can be employed to improve the performance of the passive filters.

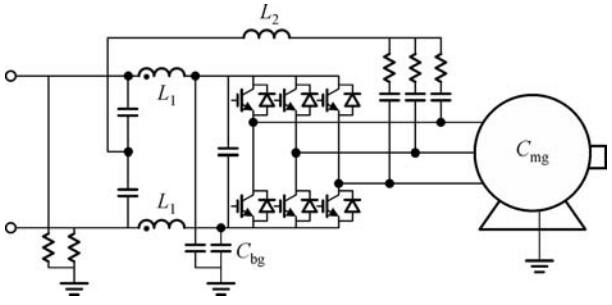

Fig. 35 Wheatstone bridge balance technique for a motor drive system in Ref. [64]

5.3 EMI noise suppression with active filters

Active filters are adopted in the noise suppression, in order to reduce the effects of passive components' parasitic parameters on the high-frequency performance of the EMI filter as well as to reduce the size. Different types of active filters have been introduced in the literature. Based on the sensing method, the active filters have the voltage and current sensing types, whereas based on the injection method, the active filters have the voltage and current compensating types. Finally, based on the position of sensing and injecting, the active filter can be divided into the feedback or feedforward types. A past study [71] propose a voltage detecting and voltage compensating circuit to eliminate the CM voltage in the system.

As shown in Fig. 37, the Y-connected capacitors between the inverter and motor provide the AC neutral voltage. The dotted line in the circuit is the active CM noise canceller (CM transformer). The AC neutral voltage is injected to the CM transformer through a push-pull emitter follower. The two series capacitors, C_0, provide a DC neutral. Given that the difference between the AC and DC neutral is the CM voltage, it is then injected to the system through the CM transformer with the same magnitude but with inverse polarities. This noise canceler

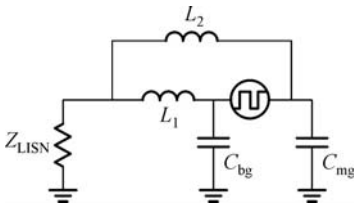

Fig. 36 Equivalent circuit with Wheatstone bridge balance applied in Ref. [64]

circuit is selected, because of its advantages, such as unity voltage gain, high-input impedance, and low-output impedance. Time-domain measurement results show a good reduction of motor terminal voltage, CM current, and shaft voltage in the system. In Ref. [74], a similar voltage sensing and voltage compensating active filter circuit has been proposed. A separated low-voltage DC power supply is used, and lower voltage/current rating transistors can be used. The capacitive voltage divider is applied at the input of the push-pull amplifier. Hence, the turns ratio of the CM transformer is no longer 1:1:1:1, which makes the total voltage gain of the active filter equal to one.

The active filter not only operates on the AC side, but it can also be applied at the DC side with both voltage cancellation and current cancellation [75]. A CM voltage cancellation technique is shown in Fig. 38(a), wherein a voltage source V_{cancel} out of phase from the noise source voltage V_{cm} is added in order to eliminate the original CM voltage source in the system. The current cancellation on the DC side is shown in Fig. 38(b). As can be seen, a current source I_{cancel} with the same magnitude but inversed direction from the noise current is generated to cancel the CM noise. Theoretically, no CM current flows through the LISNs.

Based on the voltage/current sensing point and voltage/current injection point, the active filter can be divided as feedback and feedforward cancellations, as shown in Figs. 39 and 40, respectively. In the figures, "(s)" means the Laplace form of the variables, since the system is evaluated in frequency domain.

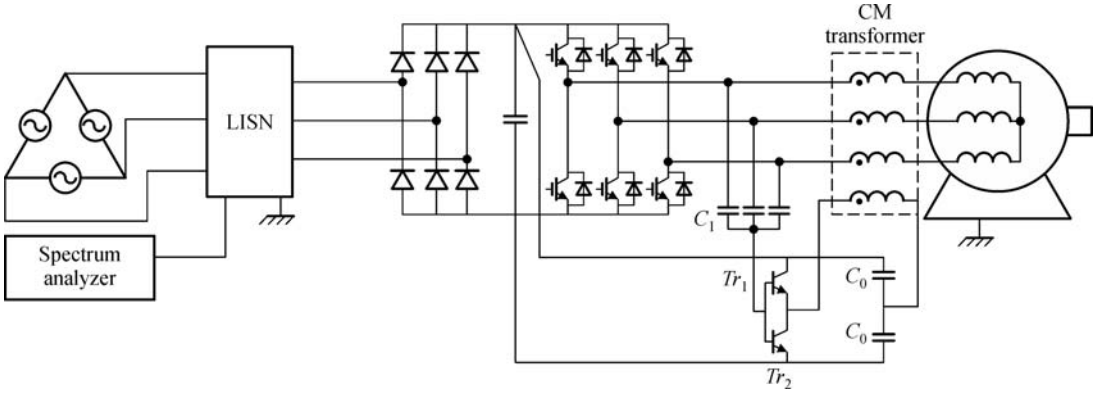

Fig. 37 A voltage-sensing voltage compensating feedback active filter

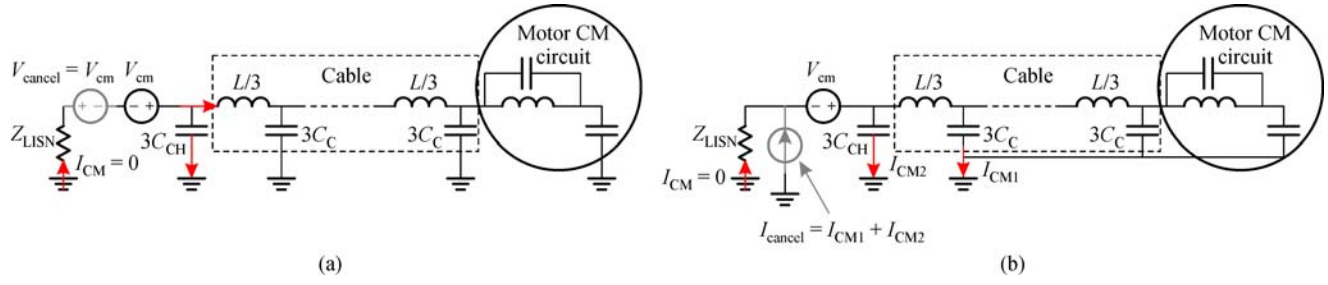

Fig. 38 Noise cancellation on the DC side. (a) Voltage cancellation; (b) current cancellation

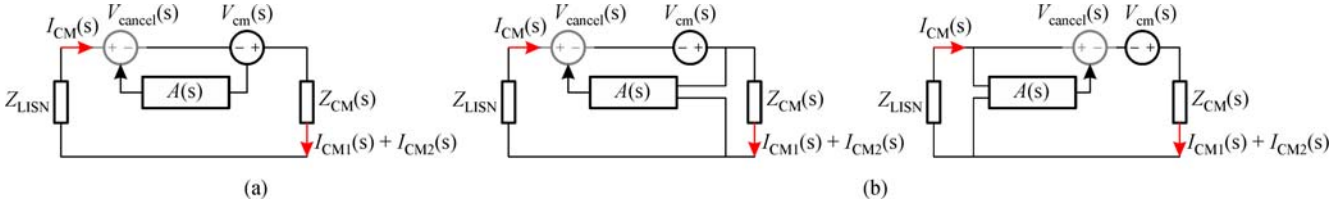

Fig. 39 Voltage-sensing and voltage-compensating equivalent circuits. (a) Feedforward; (b) feedback

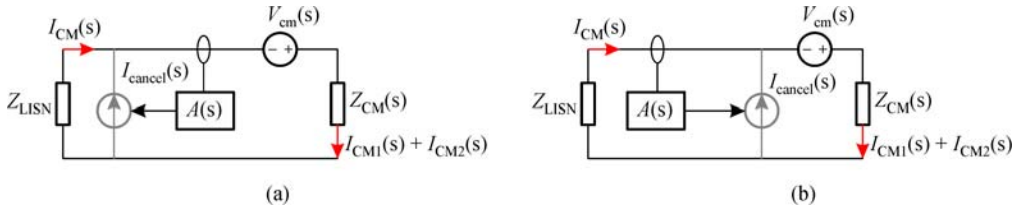

Fig. 40 Current-sensing and current-compensating equivalent circuit. (a) Feedforward; (b) feedback

In the case of a CM voltage-sensing and voltage-compensating active filters [75], a feedforward circuit is shown in Fig. 41. As can be seen, R_1 and R_2 work as the voltage dividers of the CM noise voltage, and L_p and L_s work as CM transformers to inject the voltage source with opposite phase into the system. As long as the total gain of the voltage divider, amplifier, and transformer is one, this circuit can ideally cancel the CM voltage. However, in this circuit, the transformer's size and the power loss are typically large due to the high currents in the transformer windings and high magnetizing currents. Therefore, the current cancellers are more preferred in CM cancellation.

Figure 42 shows the feedback current cancellation circuits. Here, L_p and L_s work as current transformers that sense the noise current for the active filter. If L_p/L_s equals $1/n^2$, the secondary current would be n times smaller than the original noise current. The size of the current transformer is reduced as compared with the voltage canceller. The sensed current has a voltage drop on R_1, which is the input voltage of the amplifier. The injected current has a voltage on R_2, which is then fed back to the input loop to compare with the input voltage. The injection current flows through C and flows back to the system at the center tap of two C_2, thus CM current circulates in the system without going through the LISNs.

In this paper, the optimized active filter is also discussed to increase the output current capability, reduce power loss, eliminate the HF resonances, and improve the CM noise cancellation performance. A high-performance hybrid active filter is designed, and this filter shows good CM noise reduction in a wide frequency range (10 kHz–10 MHz).

5.4 EMI Suppression with optimized modulation schemes

Given that the CM voltage is mainly generated by the high-frequency switching voltages (dv/dt), reducing the CM voltage by improving the modulation strategies without adding extra components is possible. The noise suppression modulation strategies can be divided into two conditions: 1) Reduced CM voltage PWM technique (RCMV-PWM) for three-phase voltage source inverters, and 2) modulation improvement in the rectifier-inverter system (back-to-back converter). The first type focuses on the motor inverter by using optimized RCMV-PWM. The voltage variance between each state becomes smaller than the conventional SVPWM. For the second technique, the total CM voltage is reduced in the rectifier-inverter system by the switching state shifting or the synchronous control strategy. The RCMV-PWM applied to a three-phase voltage source inverter includes the active zero-state modulation (AZSM) [87,88], remote-state modulation (RSM) [83], and near-state modulation (NSM) [90].

Zero vector is not desired in the modulation because, in

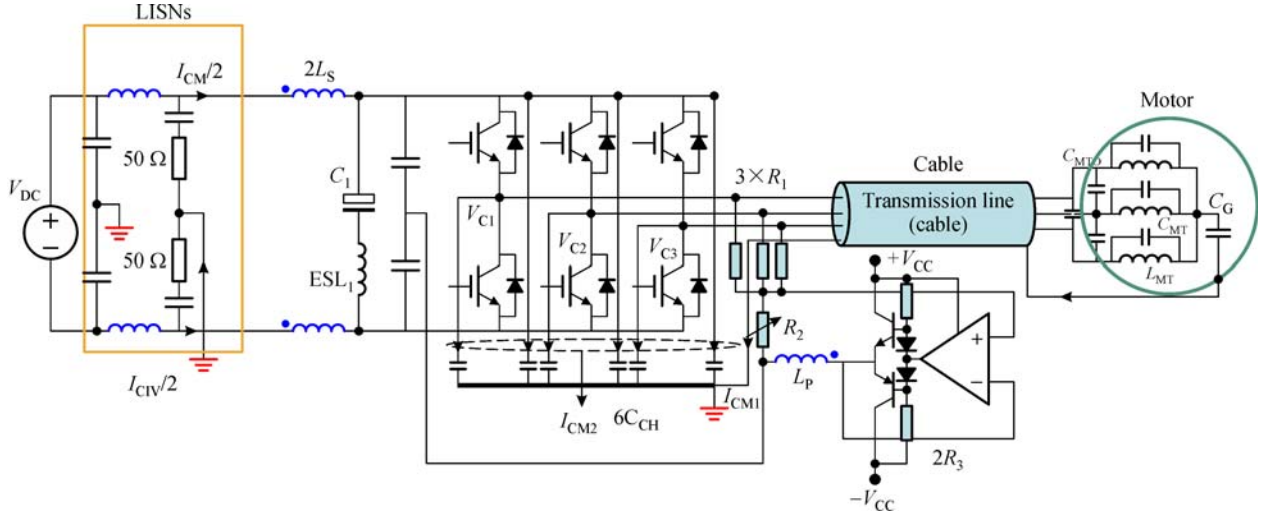

Fig. 41 A voltage-sensing and voltage-compensating feedforward active filter in Ref. [75]

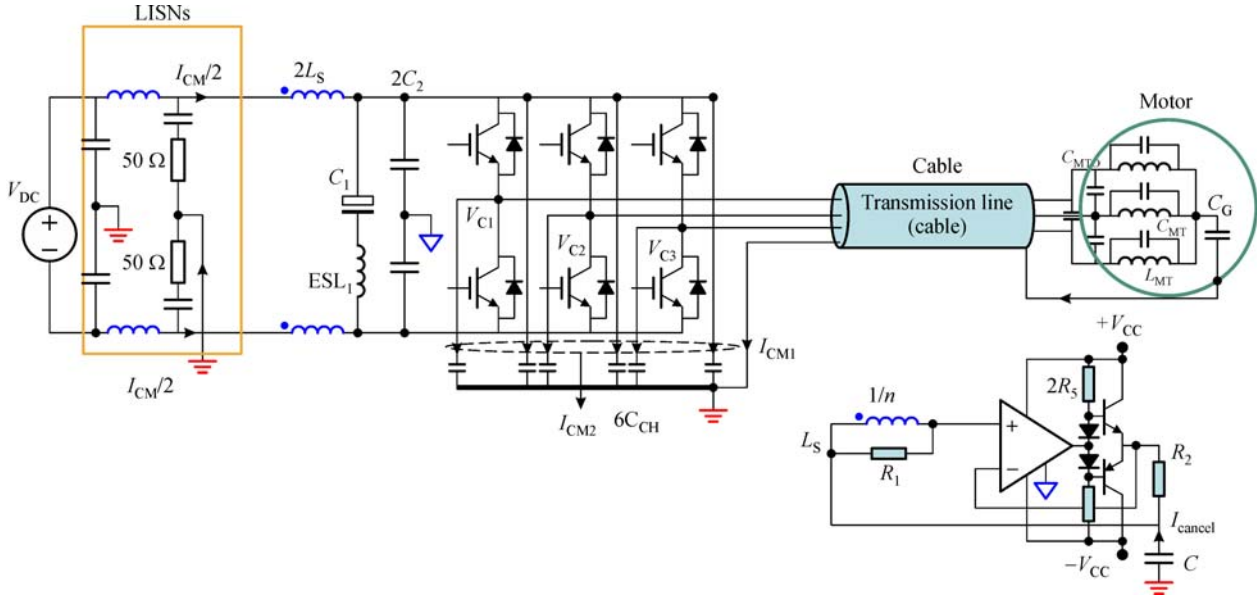

Fig. 42 A current-sensing and current-compensating feedback active filter in Ref. [75]

the conventional two-level inverters, at zero vector states (000, 111), the CM voltage has the maximum magnitude between the AC neutral and the DC mid-point ($\pm V_{dc}/2$). With the AZSM, the peak value of the CM voltage can be reduced [92]. The active zero-state basically uses other switch states to replace the conventional zero vector (000, 111) in the SVPWM. In the AZSM, as shown in Fig. 43(a), two adjacent active vectors along with the virtual zero vector (two near opposite vectors) generate a new space vector in the sections, making the volt-second of the new vector equal to the conventional SVPWM vector. Another AZSM method shown in Fig. 43(b) has three active vectors in each PWM cycle. Two vectors with opposite polarities and the remaining active vector form a new space vector. In the RSM technique, three non-adjacent state vectors (e.g., V_1, V_3, V_5) form the reference vectors V_{ref} in the modulations, whereas in the NSM, three adjacent state vectors (e.g., V_1, V_2, V_3) form the reference vector V_{ref} in the modulations. These RCMV-PWM techniques aim at constructing the reference vectors without using conventional zero state (000 and 111) in the modulations.

The RCMV-PWM can achieve a smaller CM voltage magnitude in each state ($\pm V_{dc}/6$) compared with the conventional SVPWM, thus the CM noise can be reduced.

Considering harmonic distortion factor, DC-link current harmonics, voltage linearity, etc., Ref. [89] proposed a comprehensive comparison of the above techniques. In its conclusion, the AZSM shown in Fig. 43(a) is preferred for achieving a low modulation index and low CM voltage devices. NSM is preferred for achieving a high modulation index.

These techniques concentrate on the improvement of the conventional SVPWM of the voltage source inverter. The ASD systems always operate based on a AC-DC-AC structure, or back-to-back converter or rectifier-inverter system. On the one hand, the front-end rectifier can be a diode bridge that only contributes second- or third-order harmonics of fundamental frequency. In this case, RCMV-PWM is applied to eliminate the CM voltage source. On

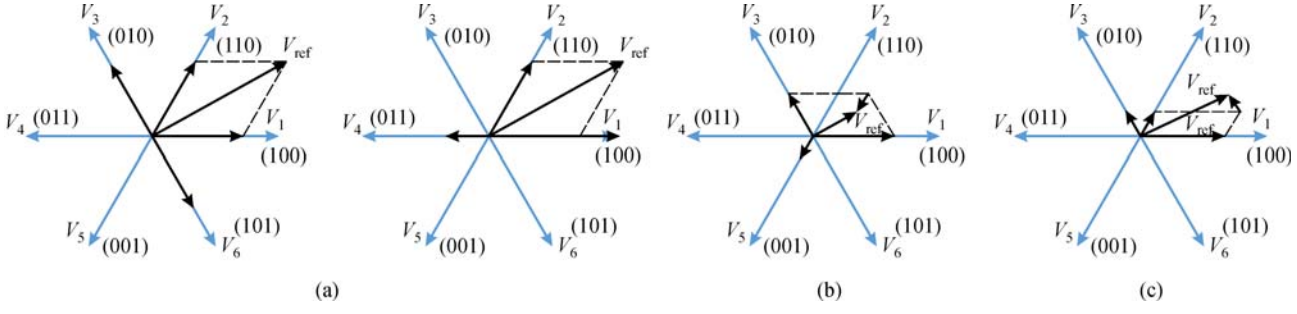

Fig. 43 RCMV-PWM in a VSI system; (a) AZSM; (b) RSM; (c) NSM

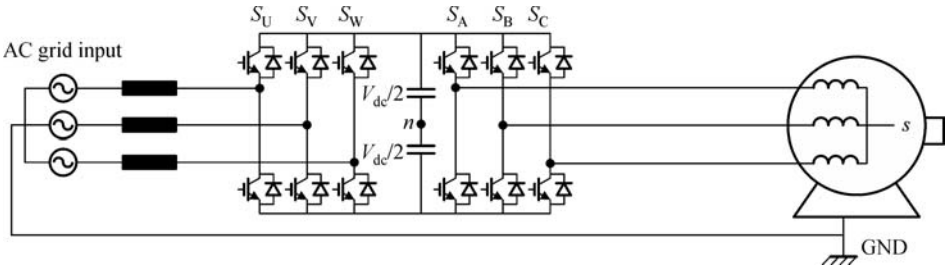

Fig. 44 An active rectifier-inverter system in Ref. [84]

the other hand, the front-end rectifier can be a controllable rectifier with active switches. For this case, past studies [84,86,93] introduced techniques to optimize the control strategy of the rectifier and inverter to reduce the CM voltage.

Another study [84] proposed an improved state-shifting SVPWM strategy for rectifier-inverter systems, as shown in Fig. 44. The rectifier and inverter can be modeled as series noise sources, and the total noise source voltage can be calculated using Eq. (5).

$$V_{cm} = \frac{V_{dc}}{6}[(S_A + S_B + S_C) - (S_U + S_V + S_W)], \quad (5)$$

where S_A, S_B and S_C represent the switch condition of each phase leg in the inverter, S_U, S_V and S_W represent the switch condition of each phase leg in the rectifier, V_{dc} represents the DC bus voltage, and V_{cm} represents the whole system's equivalent CM noise voltage source. The value of the switch conditions can only be "0" and "1". "1" means the upper switch is on and lower switch is off; and "0" means the lower switch is on and upper switch is off.

Based on the switching function of the rectifier and inverter, the total CM voltage with the relationship to the switch states of two converters is summarized in Table 1. In the table, V_0–V_7 represent the space vectors in rectifier and inverter. And V_x equals to (S_U, S_V, S_W) or (S_A, S_B, S_C). For example, V_0 equals to (S_U= 0, S_V= 0, S_W= 0) for the rectifier and (S_A= 0, S_B= 0, S_C= 0) for the inverter. And V_7 equals to (S_U= 1, S_V= 1, S_W= 1) for the rectifier and (S_A= 1, S_B= 1, S_C= 1) for the inverter.

As shown in Table 1, the maximum magnitude of the CM voltage occurs when one converter is at the state of 000 and the other is at 111. By shifting and rearranging the switching period of the inverter (or that of the rectifier), the maximum CM voltage can be avoided and a zero-voltage state can be obtained. Thus, the CM voltage has a reduced number of pulses in the same switching period. A similar method [86] has been proposed by the same authors in another study, and this method can limit the total CM voltage within $\pm V_{dc}/3$ in a synchronized rectifier-inverter system.

An improved shifting technique to fully eliminate the CM voltage theoretically is proposed in Ref. [94]. The switching states of both the rectifier and inverter can be shifted to have simultaneous rising and falling edges in the modulation. As long as the CM voltage in the inverter is exactly the same as that in the rectifier in time domain, and because they have opposite polarities in the CM noise equivalent circuit, this shifting technique can theoretically achieve full CM voltage cancellation. In the paper, the dead-time influence is considered and it is compensated to obtain good performance.

6 Conclusions

Given that motors are a complicated electromagnetic equipment in a VFD system, the EMI models of AC motors have been reviewed and discussed in detail in the literature. The physical model with the motor T model can include the load effects from the rotor side. This model extends its applied frequency range to dozen Hz. Both the magnitude and phase of the measured impedance can be modeled. However, due to the limited number of parasitic parameters included in this model, the predicted impedance curves fail to accurately match the measured impedances in the mid- and high-frequency ranges. The long cable effect is also not considered in this model. The

Table 1 CM voltage with space vectors in the rectifier-inverter systems

Boost rectifier output Spece vector	Inverter output space vector			
	V_1, V_3, V_5	V_2, V_4, V_6	V_0	V_7
V_1, V_3, V_5	0	$V_{dc}/6$	$-V_{dc}/6$	$V_{dc}/3$
V_2, V_4, V_6	$-V_{dc}/6$	0	$-V_{dc}/3$	$V_{dc}/6$
V_0	$V_{dc}/6$	$V_{dc}/3$	0	$V_{dc}/2$
V_7	$-V_{dc}/3$	$-V_{dc}/6$	$-V_{dc}/2$	0

behavior model, compared with the physical model, shows a better result in the high-frequency range. However, as it only aims at finding a circuit solution or a mathematical solution to match the measured impedance curves, it does not have any physical meaning for the motor drive system and always lacks the phase information. Even though it is accurate in the high-frequency range, it is still difficult to identify the physical characteristics in the EMI analysis.

Recently, a model combining the transmission line and the T model is proposed, including the characteristics of both the load and the long cable effect. This model matches the motor's electromagnetic performance in the low-frequency range as well as the multi-resonances due to long cable and long stator windings. This model can match both the magnitude and the phase of the measured impedances.

In the conventional CM propagation analysis, bearing and rotor models are often ignored as they do not significantly influence the CM noise current. However, EDM current and the resulting discharge current spike could damage the lubrication cream in the bearing and shorten the lifespan of the bearing. For this reason, the bearing model and the reduction of EDM current have been investigated in past studies. The noise source modeling for a rectifier inverter system have also been reviewed and discussed. With the systematic model of the VFD system, EMI noise reduction techniques are summarized and compared in this article.

Passive filters are widely used in EMI noise reduction as they are relatively easier to design compared with others. However, considering the applied voltage and current levels, the capacitors and inductors in the passive filters could be bulky and heavy, which is not a satisfactory design in a compact and integrated design. Given that the passive components also suffer from parasitic effects at high frequencies, the filter performance is greatly degraded. Sometimes, a damping circuit is needed in the passive filter to eliminate the influence of the filter's resonances.

The Wheatstone bridge balance technique can be implemented to reduce the EMI noise in the VFD system. The basic idea is to construct a circuit with four impedance branches for the noise source. In the second step, the ratios of impedance of the four branches are balanced. Theoretically the noise can be fully eliminated in this manner. However, in actual applications, the components are not ideal so the parasitic effects influence the balance at high frequencies. This technique has a good noise reduction in the low-frequency range when parasitic effects are not significant. High-frequency performance can be improved by coupling balancing inductors under some conditions.

The active filter technique is implemented to reduce the size of passive filters. A hybrid EMI filter technique can extend the filter's attenuation to a wider frequency range compared with the individual active or passive filters. Various active filter topologies can be applied to reduce the CM noise in the system. These topologies can be classified as voltage-/current-sensing, voltage-/current-compensating, and feedback/feedforward active filters. Active components, such as amplifiers and transistors are often used in the active filters. The performance of the active filter largely depends on the band width of these active components.

The optimized modulation for CM noise reduction does not need extra components in the circuit. In a single source system, AZSM is typically used to reduce the magnitude of CM voltages. In a multi-source system, the optimized modulation is applied to have the generated noise canceled. However, certain conditions must be met in using this optimized modulation technique in a multi-source system. For example, the switching frequency of two converters should be equal, and the switches in both rectifier and inverter should be triggered synchronously.

Acknowledgements This research was supported by the CRRC Zhuzhou Institute Co., Ltd.

References

1. Farnesi S, Marchesoni M, Vaccaro L. Advances in locomotive power electronic systems directly fed through AC lines. In: Proceedings of 2016 International Symposium on Power Electronics, Electrical Drives, Automation and Motion (SPEEDAM). Anacapri: IEEE, 2016, 657–664
2. Bonnett A H. Analysis of the impact of pulse-width modulated inverter voltage waveforms on AC induction motors. IEEE Transactions on Industry Applications, 1996, 32(2): 386–392
3. Kerkman R J, Leggate D, Schlegel D, et al. PWM inverters and their influence on motor overvoltage. In: Proceedings of APEC '97: Applied Power Electronics Conference and Exposition. Atlanta: IEEE, 1997, 103–113
4. Kerkman R J, Leggate D, Skibinski G L. Interaction of drive modulation and cable parameters on AC motor transients. IEEE Transactions on Industry Applications, 1997, 33(3): 722–731
5. Amarir S, Al-Haddad K. A modeling technique to analyze the impact of inverter supply voltage and cable length on industrial motor-drives. IEEE Transactions on Power Electronics, 2008, 23 (2): 753–762
6. Guastavino F, Ratto A, Torello E, et al. Aging tests on nanostructured enamels for winding wire insulation. IEEE Transactions on Industrial Electronics, 2014, 61(10): 5550–5557
7. Chen S, Lipo T A, Fitzgerald D. Source of induction motor bearing currents caused by PWM inverters. IEEE Transactions on Energy Conversion, 1996, 11(1): 25–32
8. Chen S, Lipo T A. Circulating type motor bearing current in inverter drives. IEEE Industry Applications Magazine, 1998, 4(1): 32–38
9. Erdman J M, Kerkman R J, Schlegel D W, et al. Effect of PWM inverters on AC motor bearing currents and shaft voltages. IEEE Transactions on Industry Applications, 1996, 32(2): 250–259
10. Morant A, Wisten Å, Galar D, et al. Railway EMI impact on train

operation and environment. In: Proceedings of 2012 International Symposium on Electromagnetic Compatibility (EMC EUROPE). Rome: IEEE, 2012, 1–7

11. EMC for European Railways: Study to collect and document rules, processes and procedures to verify the Electromagnetic Compatibility (EMC) of railway vehicles in Member States of the European Rail Area. 2010. Retrieved form http://www.era.europa.eu/DocumentRegister/Documents/67575_ERA_EMC_Study_Final_Report%20Issue%2005.pdf
12. Midya S, Thottappillil R. An overview of electromagnetic compatibility challenges in European Rail Traffic Management System. Transportation Research Part C: Emerging Technologies, 2008, 16(5): 515–534
13. CENELEC Standard EN 50121. Railway Applications—Electromagnetic Compatibility. 2006. Retrieved from http://standards.globalspec.com/standards/detail?docid = 10037716&familyid = EOXKUEAAAAAAAAAA
14. IEC 61800-3: 2017, Adjustable speed electrical power drive systems-Part 3: EMC requirements and specific test methods. 2012. Retrieved from https://webstore.iec.ch/publication/31003
15. Moreira A F, Lipo T A, Venkataramanan G, et al. High-frequency modeling for cable and induction motor overvoltage studies in long cable drives. IEEE Transactions on Industry Applications, 2002, 38(5): 1297–1306
16. Mirafzal B, Skibinski G L, Tallam R M, et al. Universal induction motor model with low-to-high frequency-response characteristics. IEEE Transactions on Industry Applications, 2007, 43(5): 1233–1246
17. Mirafzal B, Skibinski G L, Tallam R M. Determination of parameters in the universal induction motor model. IEEE Transactions on Industry Applications, 2009, 45(1): 142–151
18. Shin S M, Choi B H, Kang H G. Motor health monitoring at standstill through impedance analysis. IEEE Transactions on Industrial Electronics, 2016, 63(7): 4422–4431
19. Zhong E, Lipo T A. Improvements in EMC performance of inverter-fed motor drives. IEEE Transactions on Industry Applications, 1995, 31(6): 1247–1256
20. Grandi G, Casadei D, Reggiani U. Common- and differential-mode HF current components in AC motors supplied by voltage source inverters. IEEE Transactions on Power Electronics, 2004, 19(1): 16–24
21. Weber S P, Hoene E, Guttowski S, et al. Modeling induction machines for EMC-Analysis. In: Proceedings of 2004 IEEE 35th Annual Power Electronics Specialists Conference. IEEE, 2004, 94–98
22. Costa F, Vollaire C, Meuret R. Modeling of conducted common-mode perturbations in variable-speed drive systems. IEEE Transactions on Electromagnetic Compatibility, 2005, 47(4): 1012–1021
23. Moreau M, Idir N, Moigne P L, et al. Utilization of a behavioural model of motor drive systems to predict the conducted emissions. In: Proceedings of 2008 IEEE Power Electronics Specialists Conference. Rhodes: IEEE, 2008, 4387–4391
24. Kohji M, Hiroki F, Liang S. Motor modeling for EMC simulation by 3-D electromagnetic field analysis. In: Proceedings of IEEE International Electric Machines and Drives Conference. Miami: IEEE, 2009, 103–108
25. Moreau M, Idir N, Le Moigne P. Modeling of conducted EMI in adjustable speed drives. IEEE Transactions on Electromagnetic Compatibility, 2009, 51(3): 665–672
26. Luszcz J. Motor cable effect on the converter fed AC motor common-mode current. In: Proceedings of 2011 7th International Conference-Workshop Compatibility and Power Electronics (CPE). Tallinn: IEEE, 2011, 445–450
27. Degano M, Zanchetta P, Empringham L, et al. HF induction motor modeling using automated experimental impedance measurement matching. IEEE Transactions on Industrial Electronics, 2012, 59 (10): 3789–3796
28. Stevanovi I, Wunsch B, Skibin S. Behavioral high-frequency modeling of electrical motors. In: Proceedings of 2013 Twenty-Eighth Annual IEEE Applied Power Electronics Conference and Exposition (APEC). IEEE, 2013, 2547–2550
29. Sun J, Xing L. Parameterization of three-phase electric machine models for EMI simulation. IEEE Transactions on Power Electronics, 2014, 29(1): 36–41
30. Ryu Y, Park B R, Han K J. Estimation of high-frequency parameters of AC machine from transmission line model. IEEE Transactions on Magnetics, 2015, 51(3): 1–4
31. Vidmar G, Miljavec D. A universal high-frequency three-phase electric-motor model suitable for the delta-and star-winding connections. IEEE Transactions on Power Electronics, 2015, 30 (8): 4365–4376
32. Schinkel M, Weber S, Guttowski S, et al. Efficient HF modeling and model parameterization of induction machines for time and frequency domain simulations. In: Proceedings of Twenty-First Annual IEEE Applied Power Electronics Conference and Exposition. Dallas: IEEE, 2006
33. Boglietti A, Cavagnino A, Lazzari M. Experimental high-frequency parameter identification of AC electrical motors. IEEE Transactions on Industry Applications, 2007, 43(1): 23–29
34. Magdun O, Binder A. High-frequency induction machine modeling for common-mode current and bearing voltage calculation. IEEE Transactions on Industry Applications, 2014, 50(3): 1780–1790
35. Magdun O, Binder A. The high-frequency induction machine parameters and their influence on the common-mode stator ground current. In: Proceedings of XXth International Conference on Electrical Machines (ICEM). Marseille: IEEE, 2012, 505–511
36. Wang L W, Ho C N M, Canales F, et al. High-frequency modeling of the long-cable-fed induction motor drive system using TLM approach for predicting overvoltage transients. IEEE Transactions on Power Electronics, 2010, 25(10): 2653–2664
37. Boglietti A, Carpaneto E. Induction motor high frequency model. In: Proceedings of 1999 IEEE Industry Applications Conference. Thirty-Fourth IAS Annual Meeting. Phoenix: IEEE, 1999, 1551–1558
38. Zhao H, Wang S, Min J, et al. Systematic modeling for a three phase inverter with motor and long cable using optimization method. In: Proceedings of 2014 IEEE Energy Conversion Congress and Exposition (ECCE). Milwaukee: IEEE, 2016, 4696–4703
39. De Paula H, de Andrade D A, Chaves M L R, et al. Methodology

for cable modeling and simulation for high-frequency phenomena studies in PWM motor drives. IEEE Transactions on Power Electronics, 2008, 23(2): 744–752
40. Magdun O, Binder A, Purcarea C, et al. Modeling of asymmetrical cables for an accurate calculation of common-mode ground currents. In: Proceedings of 2009 IEEE Energy Conversion Congress and Exposition. San Jose: IEEE, 2009, 1075–1082
41. Chen S, Lipo T A, Fitzgerald D. Modeling of motor bearing currents in PWM inverter drives. IEEE Transactions on Industry Applications, 1996, 32(6): 1365–1370
42. Bhattacharya S, Resta L, Divan D M, et al. Experimental comparison of motor bearing currents with PWM hard and soft-switched voltage-source inverters. IEEE Transactions on Power Electronics, 1999, 14(3): 552–562
43. Wang F. Motor shaft voltages and bearing currents and their reduction in multilevel medium-voltage PWM voltage-source-inverter drive applications. IEEE Transactions on Industry Applications, 2000, 36(5): 1336–1341
44. Naik R, Nondahl T A, Melfi M J, et al. Circuit model for shaft voltage prediction in induction motors fed by PWM-based AC drives. IEEE Transactions on Industry Applications, 2003, 39(5): 1294–1299
45. Akagi H, Tamura S. A passive EMI filter for eliminating both bearing current and ground leakage current from an inverter-driven motor. IEEE Transactions on Power Electronics, 2006, 21(5): 1459–1469
46. Muetze A, Binder A. Calculation of influence of insulated bearings and insulated inner bearing seats on circulating bearing currents in machines of inverter-based drive systems. IEEE Transactions on Industry Applications, 2006, 42(4): 965–972
47. Adabi J, Zare F, Ledwich G, et al. Leakage current and common-mode voltage issues in modern AC drive systems. In: Proceedings of Australasian Universities Power Engineering Conference. Perth: IEEE, 2007, 1–6
48. Muetze A, Binder A. Calculation of motor capacitances for prediction of the voltage across the bearings in machines of inverter-based drive systems. IEEE Transactions on Industry Applications, 2007, 43(3): 665–672
49. Magdun O, Binder A. Calculation of roller and ball bearing capacitances and prediction of EDM currents. In: Proceedings of 35th Annual Conference of IEEE Industrial Electronics. Porto: IEEE, 2009, 1051–1056
50. Shami U T, Akagi H. Experimental discussions on a shaft end-to-end voltage appearing in an inverter-driven motor. IEEE Transactions on Power Electronics, 2009, 24(6): 1532–1540
51. Shami U T, Akagi H. Identification and discussion of the origin of a shaft end-to-end voltage in an inverter-driven motor. IEEE Transactions on Power Electronics, 2010, 25(6): 1615–1625
52. Fan Z, Zhi Y, Zhu B, et al. Research of bearing voltage and bearing current in induction motor drive system. In: Proceedings of 2016 Asia-Pacific International Symposium on Electromagnetic Compatibility (APEMC). Shenzhen: IEEE, 2016, 1195–1198
53. Zhang R, Wu X, Wang T. Analysis of common-mode EMI for three-phase voltage source converters. In: Proceedings of 2003 IEEE 34th Annual Power Electronics Specialist Conference. Acapulco: IEEE, 2003, 1510–1515
54. Qi T, Sun J. Common-mode EMI solutions for modular back-to-back converter systems. In: Proceedings of Twenty-Eighth Annual IEEE Applied Power Electronics Conference and Exposition (APEC). Long Beach: IEEE, 2013, 1562–1568
55. Murai Y, Kubota T, Kawase Y. Leakage current reduction for a high-frequency carrier inverter feeding an induction-motor. IEEE Transactions on Industry Applications, 1992, 28(4): 858–863
56. Ogasawara S, Akagi H. Modeling and damping of high-frequency leakage currents in PWM inverter-fed AC motor drive systems. IEEE Transactions on Industry Applications, 1996, 32(5): 1105–1114
57. Swamy M M, Yamada K, Kume T. Common-mode current attenuation techniques for use with PWM drives. IEEE Transactions on Power Electronics, 2001, 16(2): 248–255
58. Akagi H, Doumoto T. An approach to eliminating high-frequency shaft voltage and ground leakage current from an inverter-driven motor. IEEE Transactions on Industry Applications, 2004, 40(4): 1162–1169
59. Akagi H, Doumoto T. A passive EMI filter for preventing high-frequency leakage current from flowing through the grounded inverter heat sink of an adjustable-speed motor drive system. IEEE Transactions on Industry Applications, 2005, 41(5): 1215–1223
60. Akagi H, Shimizu T. Attenuation of conducted EMI emissions from an inverter-driven motor. IEEE Transactions on Power Electronics, 2008, 23(1): 282–290
61. Chen P S, Lai Y S. Effective EMI filter design method for three-phase inverter based upon software noise separation. IEEE Transactions on Power Electronics, 2010, 25(11): 2797–2806
62. Maillet Y, Lai R X, Wang S O, et al. High-density EMI filter design for DC-fed motor drives. IEEE Transactions on Power Electronics, 2010, 25(5): 1163–1172
63. Luo F, Zhang X, Boroyevich D, et al. On discussion of AC and DC side EMI filters design for conducted noise suppression in DC-fed three phase motor drive system. In: Proceedings of Twenty-Sixth Annual IEEE Applied Power Electronics Conference and Exposition (APEC). Fort Worth: IEEE, 2011, 667–672
64. Xing L, Sun J. Conducted common-mode EMI reduction by impedance balancing. IEEE Transactions on Power Electronics, 2012, 27(3): 1084–1089
65. Xue J, Wang F, Zhang X, et al. Design of output passive EMI filter in DC-fed motor drive. In: Proceedings of 2012 Twenty-Seventh Annual IEEE Applied Power Electronics Conference and Exposition (APEC). Orlando: IEEE, 2012, 634–640
66. Zhang X, Luo F, Dong D, et al. CM noise containment in a DC-fed motor drive system using DM filter. In: Proceedings of 2012 Twenty-Seventh Annual IEEE Applied Power Electronics Conference and Exposition (APEC). Orlando: IEEE, 2012, 1808–1813
67. Gong X, Josifović I, Ferreira J A. Modeling and reduction of conducted EMI of inverters with SiC JFETs on insulated metal substrate. IEEE Transactions on Power Electronics, 2013, 28(7): 3138–3146
68. Hedayati M H, Acharya A B, John V. Common-mode filter design for PWM rectifier-based motor drives. IEEE Transactions on Power Electronics, 2013, 28(11): 5364–5371
69. Zhang X, Boroyevich D, Mattavelli P, et al. EMI filter design and optimization for both AC and DC side in a DC-fed motor drive

system. In: Proceedings of Twenty-Eighth Annual IEEE Applied Power Electronics Conference and Exposition (APEC). Long Beach: IEEE, 2013, 597–603

70. Jing X, Wang F, Ben G. EMI noise mode transformation due to propagation path unbalance in three-phase motor drive system and its implication to EMI filter design. In: Proceedings of Twenty-Ninth Annual IEEE Applied Power Electronics Conference and Exposition (APEC). IEEE, 2014, 806–811
71. Ogasawara S, Ayano H, Akagi H. An active circuit for cancellation of common-mode voltage generated by a PWM inverter. IEEE Transactions on Power Electronics, 1998, 13(5): 835–841
72. Son Y C, Sul S K. A new active common-mode EMI filter for PWM inverter. IEEE Transactions on Power Electronics, 2003, 18 (6): 1309–1314
73. Son Y C, Sul S K. Generalization of active filters for EMI reduction and harmonics compensation. IEEE Transactions on Industry Applications, 2006, 42(2): 545–551
74. Di Piazza M C, Ragusa A, Vitale G. Design of grid-side electromagnetic interference filters in AC motor drives with motor-side common-mode active compensation. IEEE Transactions on Electromagnetic Compatibility, 2009, 51(3): 673–682
75. Wang S, Maillet Y Y, Wang F, et al. Investigation of hybrid EMI filters for common-mode EMI suppression in a motor drive system. IEEE Transactions on Power Electronics, 2010, 25(4): 1034–1045
76. Di Piazza M C, Ragusa A, Vitale G. An optimized feedback common-mode active filter for vehicular induction motor drives. IEEE Transactions on Power Electronics, 2011, 26(11): 3153–3162
77. Di Piazza M C, Ragusa A, Vitale G. Power-loss evaluation in CM active EMI filters for bearing current suppression. IEEE Transactions on Industrial Electronics, 2011, 58(11): 5142–5153
78. Yuen K K F, Chung H S H, Cheung V S P. An active low-loss motor terminal filter for overvoltage suppression and common-mode current reduction. IEEE Transactions on Power Electronics, 2012, 27(7): 3158–3172
79. Chen W, Yang X, Xue J, et al. A novel filter topology with active motor CM impedance regulator in PWM ASD system. IEEE Transactions on Industrial Electronics, 2014, 61(12): 6938–6946
80. Piazza M C D, Giglia G, Luna M, et al. EMI filter design in motor drives with common-mode voltage active compensation. In: Proceedings of 2014 IEEE 23rd International Symposium on Industrial Electronics (ISIE). Istanbul: IEEE, 2014, 800–805
81. Huang J, Shi H. A hybrid filter for the suppression of common-mode voltage and differential-mode harmonics in three-phase inverters with CPPM. IEEE Transactions on Industrial Electronics, 2015, 62(7): 3991–4000
82. Oriti G, Julian A L, Lipo T A. A new space vector modulation strategy for common-mode voltage reduction [in PWM invertors]. In: Proceedings of 28th Annual IEEE Power Electronics Specialists Conference. Saint Louis: IEEE, 1997, 1541–1546
83. Cacciato M, Consoli A, Scarcella G, et al. Reduction of common-mode currents in PWM inverter motor drives. IEEE Transactions on Industry Applications, 1999, 35(2): 469–476
84. Lee H D, Sul S K. A common-mode voltage reduction in boost rectifier/inverter system by shifting active voltage vector in a control period. IEEE Transactions on Power Electronics, 2000, 15 (6): 1094–1101
85. Kim H J, Lee H D, Sul S K. A new PWM strategy for common-mode voltage reduction in neutral-point-clamped inverter-fed AC motor drives. IEEE Transactions on Industry Applications, 2001, 37(6): 1840–1845
86. Lee H D, Sul S K. Common-mode voltage reduction method modifying the distribution of zero-voltage vector in PWM converter/inverter system. IEEE Transactions on Industry Applications, 2001, 37(6): 1732–1738
87. Lai Y S, Chen P S, Lee H K, et al. Optimal common-mode voltage reduction PWM technique for inverter control with consideration of the dead-time effects—Part II: Applications to IM drives with diode front end. IEEE Transactions on Industry Applications, 2004, 40(6): 1613–1620
88. Hofmann W, Zitzelsberger J. PWM-control methods for common-mode voltage minimization—A survey. In: Proceedings of International Symposium on Power Electronics, Electrical Drives, Automation and Motion. Taormina: IEEE, 2006, 1162–1167
89. Hava A M, Un E. Performance analysis of reduced common-mode voltage PWM methods and comparison with standard PWM methods for three-phase voltage-source inverters. IEEE Transactions on Power Electronics, 2009, 24(1): 241–252
90. Un E, Hava A M. A near-state PWM method with reduced switching losses and reduced common-mode voltage for three-phase voltage source inverters. IEEE Transactions on Industry Applications, 2009, 45(2): 782–793
91. Jiang D, Wang F, Xue J. PWM impact on CM noise and AC CM choke for variable-speed motor drives. IEEE Transactions on Industry Applications, 2013, 49(2): 963–972
92. Zhu N, Xu D, Wu B, et al. Common-mode voltage reduction methods for current-source converters in medium-voltage drives. IEEE Transactions on Power Electronics, 2013, 28(2): 995–1006
93. Guo X Q, Xu D, Wu B. Common-mode voltage mitigation for back-to-back current-source converter with optimal space-vector modulation. IEEE Transactions on Power Electronics, 2016, 31(1): 688–697
94. Videt A, Messaoudi M, Idir N, et al. PWM strategy for the cancellation of common-mode voltage generated by three-phase back-to-back inverters. IEEE Transactions on Power Electronics, 2017, 32(4): 2675–2686
95. Wang S, Kong P, Lee F C. Common-mode noise reduction for boost converters using general balance technique. IEEE Transactions on Power Electronics, 2007, 22(4): 1410–1416
96. 112-1996—IEEE Standard Test Procedure for Polyphase Induction Motors and Generators. IEEE Standard 112-2004, 2004
97. Zhang H, Yang L, Wang S, et al. Common-mode EMI noise modeling and reduction with balance technique for three-level neutral point clamped topology. IEEE Transactions on Industrial Electronics, 2017, 64(9): 7563–7573
98. Robutel R, Martin C, Buttay C, et al. Design and implementation of integrated common-mode capacitors for SiC-JFET inverters. IEEE Transactions on Power Electronics, 2014, 29(7): 3625–3636
99. Xue J, Wang F, Guo B. EMI noise mode transformation due to propagation path unbalance in three-phase motor drive system and its implication to EMI filter design. In: Proceedings of 2014 IEEE

Applied Power Electronics Conference and Exposition—APEC 2014. 2014, 806–811

100. Wang S, van Wyk J D, Lee F C. Effects of interactions between filter parasitics and power interconnects on EMI filter performance. IEEE Transactions on Industrial Electronics, 2007, 54(6): 3344–3352
101. Yang L, Wang S. A compensation winding structure for balanced three-phase coupled inductor. In: Proceedings of 2017 IEEE Applied Power Electronics Conference and Exposition (APEC). Tampa: IEEE, 2017, 868–875
102. Wang S. EMI Reduction Techniques for Power Electronics Systems. Professional seminar slides. 2015. Retrieved from http://www.elitetest.com/sites/default/files/downloads/seminar_2015_trifold.pdf
103. Shih F Y, Chen D Y, Wu Y P, et al. A procedure for designing EMI filters for AC line applications. IEEE Transactions on Power Electronics, 1996, 11(1): 170–181
104. Jiao Y, Lee F C. LCL filter design and inductor current ripple analysis for a three-level NPC grid interface converter. IEEE Transactions on Power Electronics, 2015, 30(9): 4659–4668
105. Boillat D O, Kolar J W, Hlethaler M J. Volume minimization of the main DM/CM EMI filter stage of a bidirectional three-phase three-level PWM rectifier system. In: Proceedings of Energy Conversion Congress and Exposition (ECCE). Denver: IEEE, 2013, 2008–2019
106. Wang S, Chen R, van Wyk J D, et al. Developing parasitic cancellation technologies to improve EMI filter performance for switching mode power supplies. IEEE Transactions on Electromagnetic Compatibility, 2005, 47(4): 921–929
107. Wang S, Lee F C. Common-mode noise reduction for power factor correction circuit with parasitic capacitance cancellation. IEEE Transactions on Electromagnetic Compatibility, 2007, 49(3): 537–542
108. Wang S, Lee F C, Odendaal W G. Characterization and parasitic extraction of EMI filters using scattering parameters. IEEE Transactions on Power Electronics, 2005, 20(2): 502–510
109. Xing L, Sun J. Optimal damping of multistage EMI filters. IEEE Transactions on Power Electronics, 2012, 27(3): 1220–1227
110. Nakamura K, Honma K, Ohinata T, et al. Development of concentric-winding type three-phase variable inductor. IEEE Transactions on Magnetics, 2015, 51(11): 1–4
111. Liu Y, See K Y, Tseng K J, et al. Magnetic integration of three-phase LCL filter with delta-yoke composite core. IEEE Transactions on Power Electronics, 2017, 32(5): 3835–3843
112. Khan A A, Cha H, Kim H G. Three-phase three-limb coupled inductor for three-phase direct PWM AC-AC converters solving commutation problem. IEEE Transactions on Industrial Electronics, 2016, 63(1): 189–201